

Hyperons in neutron stars and supernova cores

Micaela Oertel¹, Francesca Gulminelli², Constança Providência³, and Adriana R. Raduta⁴

¹ LUTH, CNRS, Observatoire de Paris, Université Paris Diderot, 5 place Jules Janssen, 92195 Meudon, France

² ENSICAEN, UMR6534, LPC, F-14050 Caen cédex, France

³ CFisUC, Department of Physics, University of Coimbra, Portugal

⁴ IFIN-HH, Bucharest-Magurele, POB-MG6, Romania

Received: date / Revised version: date

Abstract. The properties of compact stars and their formation processes depend on many physical ingredients. The composition and the thermodynamics of the involved matter is one of them. We will investigate here uniform strongly interacting matter at densities and temperatures, where potentially other components than free nucleons appear such as hyperons, mesons or even quarks. In this paper we will put the emphasis on two aspects of stellar matter with non-nucleonic degrees of freedom. First, we will study the phase diagram of baryonic matter with strangeness, showing that the onset of hyperons, as that of quark matter, could be related to a very rich phase structure with a large density domain covered by phase coexistence. Second, we will investigate thermal effects on the equation of state (EoS), showing that they favor the appearance of non-nucleonic particles. We will finish by reviewing some recent results on the impact of non-nucleonic degrees freedom in compact star mergers and core-collapse events, where thermal effects cannot be neglected.

PACS. PACS-key describing text of that key – PACS-key describing text of that key

1 Introduction

The properties of compact stars, their formation processes as well as binary mergers depend on many different physical ingredients, among them the thermodynamic properties of the involved matter entering via the equation of state (EoS). There is an intrinsic connection between the properties of matter contained in the EoS for the macroscopic description of astrophysical objects and the underlying fundamental interactions between particles on the microscopic level. This makes the study of the aforementioned systems very rewarding as they challenge our understanding of nature on both scales.

It is not an obvious task to construct such an EoS. The main difficulty arises from the fact that very large ranges of (baryon number) densities ($10^{-10} \text{ fm}^{-3} \lesssim n_B \lesssim 1 \text{ fm}^{-3}$), temperatures ($0 < T \lesssim 150 \text{ MeV}$) and hadronic charge fractions ($0 < Y_Q = n_Q/n_B \lesssim 0.7$) have to be covered. n_Q here denotes the total hadronic charge density, which in many cases is just given by the proton density. Within this range, the characteristics of matter change dramatically, from an ideal gas of different nuclei up to uniform strongly interacting matter, containing in the simplest case just free nucleons and potentially other components such as hyperons, nuclear resonances or mesons. Even a transition to deconfined quark matter cannot be excluded.

For core collapse matter, the full density, temperature, and Y_q -dependence have to be included within the EoS. This complexity is the main reason why until recently only a few hadronic EoSs existed for core collapse simulations. These are the one by Hillebrandt and Wolff [1], used by some groups performing supernova simulations, that by Lattimer and Swesty [2] and finally that by H. Shen *et al.* [3]. The two latter, publicly available, are most commonly used in core-collapse simulations. They use different nuclear interactions, but are based on the same limiting assumptions: they take into account non-interacting α -particles, a single heavy nucleus and free nucleons in addition to the electron, positron and photon gas.

In recent years, several new models have been constructed, enlarging the variety of nuclear interaction models. This helps to estimate the uncertainty on astrophysical simulations induced by our limited knowledge about the interaction in hot and dense matter. Apart from employing different models, the full nuclear distribution at sub-nuclear densities has been included within different approaches (see e.g. [4, 5, 6, 7, 8, 9, 10]), showing considerable differences to that obtained via the single nucleus approximation in the standard EoS employed in core collapse simulations [2, 3].

Up to now, much less effort has been devoted to the high density ($n_B \gtrsim n_0$) and high temperature ($T \gtrsim 20 \text{ MeV}$) part of the EOS, including additional particles, such as hyperons and mesons or quarks. One reason might be

that the recent observation of two neutron stars with a mass of about $2M_{\odot}$ [11,12] has triggered intensive discussion on the composition of matter in the central part of neutron stars and its EoS, excluding in the standard picture additional degrees of freedom in super-saturation matter, i.e. at densities above a baryon number density of $n_0 \approx 0.16 \text{ fm}^{-3}$, since they lead to a considerable softening of the EoS [13]. This observation, however, does not exclude them, but only puts stringent constraints on the respective interaction (e.g. [14,15,16,17,18,19,20,21,22,23,24,25,26]). Different solutions with hyperonic and/or quark matter have been proposed without any definite conclusion.

In addition, even if it turns out that finally in cold neutron stars only nucleonic matter is present, in stellar core-collapse events and neutron star mergers, matter is strongly heated in addition to being compressed to densities above nuclear matter saturation density. The temperatures and densities reached can become so high that a traditional description in terms of electrons, nuclei, and nucleons is no longer adequate. Compared with the cold neutron star EoS, temperature effects favor the appearance of additional particles such as pions and hyperons and they become abundant in this regime. A transition to quark matter is possible, too [27].

The opening of additional degrees of freedom in dense matter could happen smoothly or could be accompanied by a phase transition with a considerable effect on the thermodynamics and the hydrodynamical evolution of the system, see e.g. [27]. In this context, the best known example is the hadron-quark phase transition, expected to be first order within the density and temperature range relevant for compact stars and core-collapse supernovae, see e.g. the contribution by A. Sedrakian to this issue [28]. In practice, anyway, the hadronic and the quark phases are described within different models, the transition necessarily shows discontinuities in the thermodynamic quantities. It is less known that the appearance of hyperons could be associated with a “strangeness driven” phase transition, too, similar to the liquid-gas transition in nuclear matter. A detailed study of the phase diagram of the n, p, Λ -system was recently undertaken in Refs. [29,30] within a non-relativistic mean-field model based on phenomenological functionals. It was shown that under these assumptions first- and second- order phase transition exist, and are expected to be explored under the strangeness equilibrium condition characteristic of stellar matter. In Refs. [31,26] a phase transition at the onset of hyperons has been discussed for relativistic mean field models, however in a model with very strong YY attraction.

Within this paper, we want to address two aspects of the EoS of super-saturation matter. First, we will investigate the influence of a possible phase transition at the respective hyperonic thresholds on the phase diagram of super-saturation baryonic matter and discuss possible astrophysical consequences. We will not discuss the question whether hyperonic interactions lead to such a phase transition or not, see e.g. [32] for a thorough study of that point, but just assume that it exists and explore the pos-

sible consequences. Second, we will, independently of the way they appear, discuss different works on the super-saturation EoS including additional particles with an emphasis on thermal effects. The cold neutron star part will be discussed in other contributions to this issue [33]. We will mention astrophysical applications, too, discussing in particular the impact of additional particles on black hole formation.

This paper is organized as follows: in Sec. 2, we review the main features of the thermodynamic analysis of the phase diagram of a \mathcal{N} -component system, and the phase diagram of baryonic matter with strangeness is discussed, in particular, a possible strangeness driven phase transition and the Coulomb effects on the phase diagram; in Sec. 3 thermal effects on the EoS including non-nucleonic degrees of freedom are presented, we review relativistic mean field models for the EoS, including the hyperonic interaction, and discuss the effect of including hyperons and pions in the finite temperature EoS; in Sec. 4 the impact of additional particles in astrophysical applications is referred and finally in the last section some conclusions are drawn.

2 A possible strangeness-driven phase transition?

2.1 Thermodynamic analysis of the phase diagram

In this section we would like to recall the main features of the thermodynamic analysis of the phase diagram, see e.g. [34]. The phase diagram of a \mathcal{N} -component system is, at constant temperature, a \mathcal{N} -dimensional volume. If there are M different coexisting phases, the boundaries of the phase coexistence domain(s), $\{n_i^{P_j}\}$; $i = 1, \dots, \mathcal{N}$; $j = 1, \dots, M$, are determined by the $(\mathcal{N} + 1)(M - 1)$ conditions of thermodynamic equilibrium between them,

$$\begin{aligned} \left(\frac{\partial f}{\partial n_i}\right)_{P_1} &= \dots = \left(\frac{\partial f}{\partial n_i}\right)_{P_M} = \mu_i; \quad i = 1, \dots, \mathcal{N} \\ \left(-f + \sum_i n_i \frac{\partial f}{\partial n_i}\right)_{P_1} &= \dots = \left(-f + \sum_i n_i \frac{\partial f}{\partial n_i}\right)_{P_M} = P, \end{aligned} \quad (1)$$

where f denotes the free energy density and P the pressure. Within the phase coexistence domain(s), a mixture of different phases lowers the free energy of the system as compared with the solutions corresponding to individual phases. Mathematically, this is equivalent to the presence of a convexity anomaly of the thermodynamic potential in the density hyperspace, i.e. the free energy curvature matrix, $C_{ij} = \partial^2 f / \partial n_i \partial n_j$, has at least one negative eigenvalue. The number of coexisting phases is determined by the number of order parameters¹ or, in terms

¹ An order parameter is defined here as the direction in the observable space corresponding to phase separation, see e.g. Ref. [35] for details

of local properties, by the number of directions in density space where spinodal instabilities develop, i.e. where density fluctuations are spontaneously amplified finally leading to phase separation. The latter quantity is related to the number \mathcal{N}_{neg} of negative eigenvalues of C_{ij} , such that $M = \mathcal{N}_{neg} + 1$.

If the direction of phase separation is unique, which corresponds to a one-dimensional order parameter, then the problem of phase coexistence in a \mathcal{N} -component system can be reduced to a problem of phase coexistence in a one-component system by Legendre transforming the thermodynamical potential f with respect to the remaining $(\mathcal{N} - 1)$ -chemical potentials [36].

Baryonic matter with hyperons contains eight different particle species. Under the condition of equilibrium with respect to the strong interaction, the number of relevant degrees of freedom is, however, reduced to three, the densities baryon number density n_B , the total baryonic (electric) charge density n_Q and the total strangeness density n_S . It represents, therefore, a three-component system in the terminology introduced above ² It is important to remark here that the use of strangeness as a relevant degree of freedom does not imply that n_S is conserved throughout the evolution of the system. In particular, along the strangeness equilibrium trajectory $\mu_S = 0$ considered in this study, n_S obviously varies. Upon adding leptonic degrees of freedom in form of electrons and positrons, (electron) lepton number enters as an additional variable. Due to the strict electrical neutrality condition, however, charge is no longer an independent degree of freedom once leptons are included and the system remains three-dimensional [38, 30], see also Ref. [39], in terms of the number densities n_B, n_S and n_L . In the absence of neutrinos, n_L , the electron lepton density, denotes here the net electron density, $n_L = n_e = n_{e^-} - n_{e^+}$ and charge neutrality gives $n_L = n_Q$.

The equilibrium conditions thus reduce the dimensionality of the phase space from 8 (9 with electrons), corresponding to the number of different particle species, to three, described by baryon, lepton and strangeness number densities. To further reduce the dimensionality for studying phase coexistence, one may then perform the Legendre transformation with respect to any set (μ_B, μ_S) , $(\mu_S, \mu_{Q(L)})$ and $(\mu_B, \mu_{Q(L)})$. $\mu_{Q(L)}$ thereby stands either for μ_Q in a purely baryonic systems or for μ_L if electrons are included. In practice, we found that the order parameter is always one dimensional. This means that a single Legendre transformation is enough to spot the thermodynamics provided that the order parameter is not orthogonal to the controlled density. The most convenient framework to easily access the physical trajectories is the one controlling the n_B -density:

$$\bar{f}(n_B, \mu_S, \mu_{Q(L)}) = f(n_B, n_S, n_{Q(L)}) - \mu_S n_S - \mu_{Q(L)} n_{Q(L)}. \quad (2)$$

Coexisting phases, if any, will then be characterized by equal values of $\mu_B = \partial \bar{f} / \partial n_B$ and P and the phase in-

stability regions will be characterized by a back-bending behavior of $\mu_B(n_B)|_{\mu_S, \mu_{Q(L)}}$.

2.2 The phase diagram of baryonic matter with strangeness

Due to the large incompressibility of electrons present to ensure electrical charge neutrality, Coulomb interactions can have a considerable influence on the phase diagram, in particular if charged particles are involved. For instance, the well known nuclear liquid-gas phase transition is strongly quenched by Coulomb effects [36, 40, 41]. On the contrary, in Ref. [30] it has been shown that, if Λ -hyperons are the only strange baryons, the supra-saturation phase transition occurring in the $np\Lambda + e$ -system is only slightly modified by Coulomb interactions compared with the $np\Lambda$ -system. The reason is that this phase transition is “strangeness driven”, i.e. the order parameter is dominated by n_S and has only a small component in direction of the charge. On the other hand, if the hyperonic couplings are such that charged hyperons are abundant, as predicted by many models favoring negatively charged hyperons, the extension and localization of phase coexistence domains could be strongly modified by the Coulomb interaction. In the extreme case, it could even make it disappear for neutron star matter.

For the present study we will employ the non-relativistic energy density functional developed by Balberg and Gal [42], which is known to present a rich phase structure [29, 30]. The total baryonic energy density is then given by the sum of mass, kinetic and potential energy density,

$$e_B = \sum_{i=n,p,Y} \left(n_i m_i c^2 + \frac{\hbar^2}{2m_i} \tau_i \right) + e_{pot}(\{n_i\}). \quad (3)$$

The single-particle densities and kinetic energy densities are thereby given by the Fermi integrals

$$n_i = \frac{4\pi}{h^3} \left(\frac{2m_i}{\beta} \right)^{\frac{3}{2}} F_{\frac{1}{2}}(\beta \tilde{\mu}_i); \quad \tau_i = \frac{8\pi^3}{h^5} \left(\frac{2m_i}{\beta} \right)^{\frac{5}{2}} F_{\frac{3}{2}}(\beta \tilde{\mu}_i), \quad (4)$$

with $F_\nu(\eta) = \int_0^\infty dx \frac{x^\nu}{1 + \exp(x - \eta)}$ being the Fermi-Dirac integral, $\beta = T^{-1}$ is the inverse temperature, m_i denotes the i -particle mass and $\tilde{\mu}_i$ the effective chemical potential of particle species i -species.

The potential energy density proposed by Balberg and Gal [42] has the following form,

$$e_{pot}^{(BG)}(\{n_i\}) = \sum_{i,j} e_{ij}^{(BG)}(n_i, n_j);$$

$$e_{ij}^{(BG)}(n_i, n_j) = \left(1 - \frac{\delta_{ij}}{2} \right) (a_{ij} n_i n_j + b_{ij} n_i n_j^3 + c_{ij} \frac{n_i^{\gamma_{ij}+1} n_j + n_j^{\gamma_{ij}+1} n_i}{n_i + n_j}), \quad (5)$$

For simplicity the same functional form is employed in all channels and a unique value is used for the exponent governing the short-range repulsion. The values of the coupling

² See Ref. [37] for a discussion of the phase diagram if strong equilibrium is not assumed.

constants, listed in Table 1, have been chosen to satisfy the experimental constraints available at that time, symmetry arguments or, in the case of the NN -channel, to agree with popular models. Concerning the latter, the resulting values are in good agreement with experimental constraints for the saturation density, $n_0 = 0.155 \text{ fm}^{-3}$, and energy per nucleon of symmetric nuclear matter at saturation, -15.9 MeV . The incompressibility modulus with 375 MeV is, instead, largely overestimated. The well depths of various hyperonic species in uniform symmetric nuclear matter at saturation density are: $U_{\Lambda}^{(N)}(n_0) = U_{\Sigma}^{(N)}(n_0) = -26.6 \text{ MeV}$, $U_{\Xi}^{(N)}(n_0) = -22.8 \text{ MeV}$ and the value of Λ -potential in Λ -matter $U_{\Lambda}^{(\Lambda)}(n_0/5) = -12.8 \text{ MeV}$. Both, the ΞN - and $\Lambda\Lambda$ -potentials are too attractive in view of actual experimental data. AGS-E885 data indicate for $U_{\Xi}^{(N)}(n_0)$ the value of -14 MeV [43]. The value of $U_{\Lambda}^{(\Lambda)}(n_0/5)$ can be related to the bond energy of double- Λ hypernuclei [44]. Experimental data for ${}_{\Lambda\Lambda}^6\text{He}$ [45] suggest that a much larger value of $U_{\Lambda}^{(\Lambda)}(n_0/5) = -0.67 \text{ MeV}$ is more realistic. The situation of the ΣN -potential is ambiguous but, very probably, it is repulsive. Alternative values of the coupling constants which overcome the drawbacks of the original parameterization have been proposed in Ref. [20].

Thermodynamic consistency allows to infer the relation between the chemical potentials $\mu_i \equiv \partial e_B / \partial n_i|_{n_j, j \neq i}$ and the effective ones $\tilde{\mu}_i$ as $\mu_i = \tilde{\mu}_i + m_i c^2 + U_i$, with $U_i = \partial e_{\text{pot}} / \partial n_i$. All remaining thermodynamic quantities, such as pressure or entropy can then be derived from the energy density via standard thermodynamic relations.

2.2.1 The n, p, Y -system without electrons

In order to highlight the effect of the Coulomb interaction, we will start within this section by analyzing the phase diagram of pure baryonic matter including the complete baryon octet, but without electrons. The upper panel of Fig. 1 illustrates the evolution of the baryonic chemical potential as a function of baryon number density at constant values of $\mu_S = 0$, $\mu_Q = 0$ and $T = 1 \text{ MeV}$ ³. Three back-bending regions exist, which are all correlated with a particle threshold, see the bottom panel of Fig. 1 where the corresponding particle abundances are displayed. Since within the model of Balberg and Gal [42] the hyperon-hyperon (YY)-interaction depends only weakly on the particular channel, the order of the particle thresholds is mainly given by their respective rest masses and chemical potentials. In the present case, $\mu_S = \mu_Q = 0$, this means that the Λ is the first one to appear, followed by the almost degenerate Σ -hyperons and then the Cascades. An investigation of $\tilde{f}(n_B)$ confirms that any back-bending can be cured by a Maxwell construction and that the mixture of stable phases lowers the free energy compared with the individual phases and corresponds thus to the energetically favored solution. This means that three distinct

³ This temperature value has been chosen for computational convenience. The presented results are very close to the zero temperature limit.

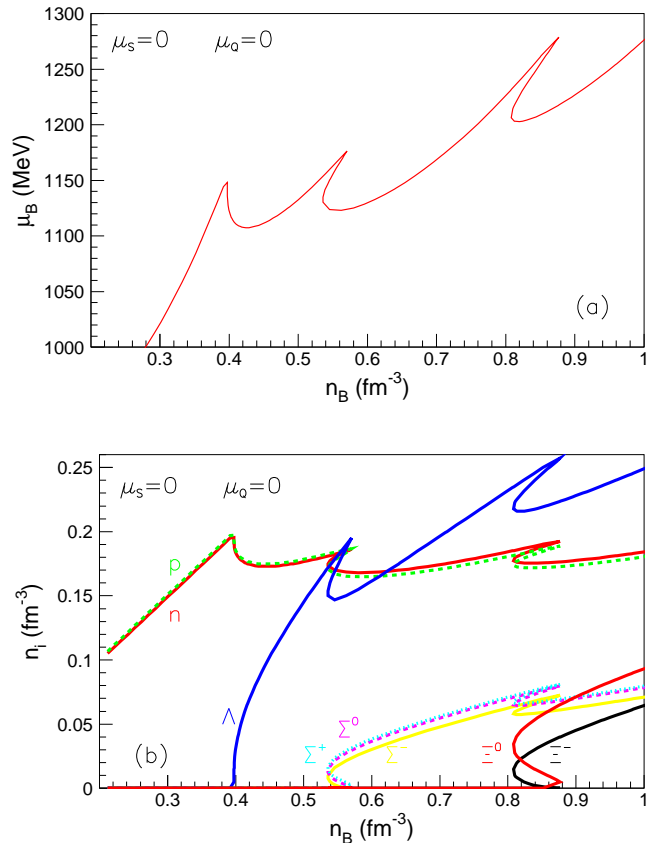


Fig. 1. (Color online) Baryonic chemical potential (top) and particle abundances (bottom) as a function of baryon number density for $\mu_S = 0$ and $\mu_Q = 0$ at $T = 1 \text{ MeV}$, employing the BGI parameterization [42].

phase coexistence regions exist, induced by the onset of each hyperonic family.

Different thermodynamical conditions, i.e. different values of (μ_S, μ_Q) and T , will obviously change the particle thresholds, their abundances, and the location of phase coexistence regions. By varying μ_S and μ_Q , the whole 3-dimensional phase diagram for a given temperature could be explored. Since we are mostly interested here in astrophysical systems which can be considered in strangeness changing weak equilibrium, $\mu_S = 0$, we will limit the analysis to this case. The corresponding projections of the phase diagram on the n_B - n_Q (panel (a)) and the n_S - n_Q -plane (panel (b)) are represented in Fig. 2. The arrows indicate the directions of phase separation. In general, increasing μ_Q leads to higher values of n_Q . The $\mu_Q = 0$ trajectory considered in Fig. 1 is here represented with dashed lines. For the sake of completeness, also the phase coexistence region of the (n, p, Λ) systems at supra-saturation densities is illustrated as a hatched yellow area [29, 30].

Most of the time, the phase coexistence domains related to the onset of Λ - and Σ -hyperons merge to a single domain extending over a very large range of baryon num-

Table 1. Coupling constants corresponding to the stiffest interaction proposed in Ref. [42], called BGI within this paper, and those corresponding to the nuclear interaction used by Lattimer and Swesty [2] supplemented with the Λ -hyperon [30,46]. In case of BGI, the only hyperon pair with non-vanishing isospin-component is Σ - Σ .

Parameter set	a_{NN} MeV fm ³	b_{NN} MeV fm ³	c_{NN} MeV fm ^{3γ_{NN}}	a_{AA} MeV fm ³	b_{AA} MeV fm ³	c_{AA} MeV fm ^{3γ_{AA}}	a_{AN} MeV fm ³	b_{AN} MeV fm ³	c_{AN} MeV fm ^{3γ_{AN}}	γ_{NN}	γ_{AN}	γ_{AA}
BGI	-784.4	214.2	1936.0	-486.2	0	1553.6	-340.0	0	1087.5	2	2	2
LS220A	-1636.2	214.2	1869.2	-486.2	0	1553.6	-340.0	0	1087.5	1.26	2	2
220g3	-1636.2	214.2	1869.2	-90.0	0	1000.0	-270.0	0	4000.0	1.26	3	3

Parameter set	$a_{\Sigma N}$ MeV fm ³	$b_{\Sigma N}$ MeV fm ³	$c_{\Sigma N}$ MeV fm ^{3$\gamma_{\Sigma N}$}	$a_{\Xi N}$ MeV fm ³	$b_{\Xi N}$ MeV fm ³	$c_{\Xi N}$ MeV fm ^{3$\gamma_{\Xi N}$}	$a_{\Upsilon\Upsilon}$ MeV fm ³	$b_{\Upsilon\Upsilon}$ MeV fm ³	$c_{\Upsilon\Upsilon}$ MeV fm ^{3$\gamma_{\Upsilon\Upsilon}$}	$\gamma_{\Sigma N}$	$\gamma_{\Xi N}$	$\gamma_{\Upsilon\Upsilon}$
BGI	-340.0	214.2	1087.5	-291.5	0	932.5	a_{AA}	0/428.4	c_{AA}	2	2	2
220g3	450.0	214.2	250.0	-170.0	0.0	2900.0	a_{AA}	0/430.0	c_{AA}	3	3	3

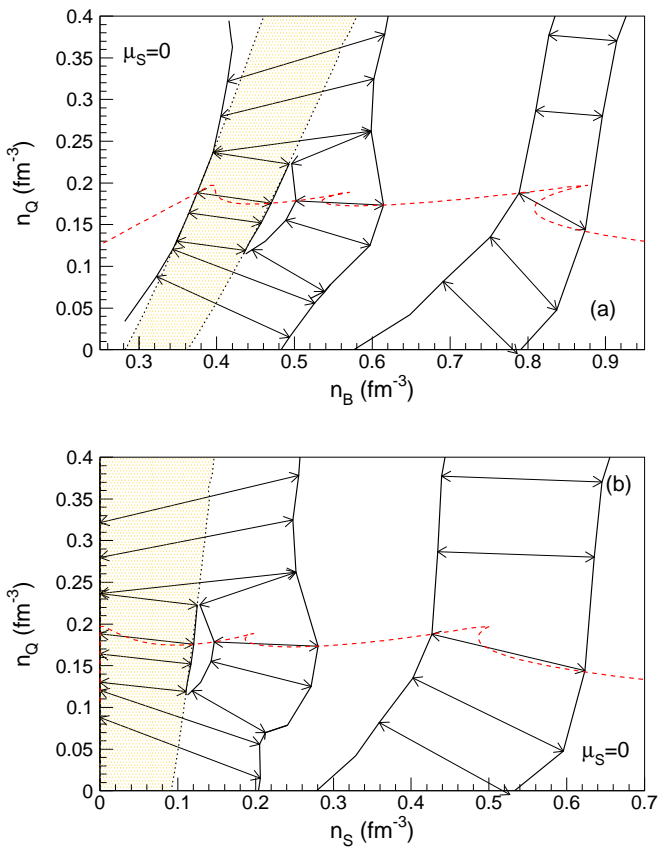


Fig. 2. (Color online) Phase diagram of the (n, p, Y) -system for $\mu_S = 0$ at $T=1$ MeV as provided by the BGI parameterization [42] in the n_B - n_Q (a) and n_S - n_Q (b) planes. The arrows indicate the directions of phase separation. The $\mu_Q = 0$ trajectory is illustrated with a red dashed line. The hatched yellow area corresponds to the strangeness driven phase transition domain of the simpler (n, p, Λ) -system studied in Ref. [30].

ber density, whereas the Cascade thresholds remain separated leading to a second distinct phase transition region. This can be understood as follows: nonzero values of μ_Q , positive or negative, lift the degeneracy of the Σ -hyperons, favoring the appearance of charged ones, negative or positive depending on the sign of μ_Q . The corresponding threshold for Σ^+ or Σ^- is shifted to lower densities with

increasing absolute value of μ_Q , closer to the threshold of neutral Λ -hyperons. At some critical value, the two phase coexistence regions existing at $\mu_Q = 0$ merge into one single domain.

As expected, the component of the order parameter in n_Q -direction is more important if the number of charged particles participating in the phase coexistence is large, i.e. for large values of μ_Q . In fact, although the total charge n_Q is rather small for large μ_Q , the abundances of charged baryons itself are large. For instance, the transition induced by Λ - and Σ -hyperons shows an almost vanishing component in n_Q -direction close to $\mu_Q = 0$, where three phase coexistence regions exist and the Σ -onset is almost degenerate, see Fig. 2, whereas it becomes larger with increasing $|\mu_Q|$, i.e. in the regions where only two phase coexistence domains exist. The Ξ -induced phase transition has an order parameter with important contribution along n_Q whenever both Ξ^0 and Ξ^- are created as their total charge cannot vanish. With increasing μ_Q the Ξ^- production threshold is shifted to higher densities, finally leaving the considered density domain. Consequently, the charge dependence of the order parameter becomes very weak for large n_Q .

2.2.2 Coulomb effects on the phase diagram

We now turn to investigate the influence of Coulomb effects on the phase diagram. For simplicity, we will consider only electrons and neglect other charged leptons or mesons. The total free energy can be written as the sum of a baryonic, leptonic and photonic contribution, $f = f_B + f_L + f_\gamma$, where leptons and baryons are coupled only via the strict electrical neutrality condition, $n_Q = n_L$. Leptons and photons are well described by, respectively, fermionic and bosonic ideal gases [2]. None of them affects the phase structure.

In the case of the n, p, Λ -system, where the order parameter has only a small component in charge direction, the effect of electrons on the phase diagram is small [30]. As discussed in the previous section, upon including the full octet with all charged hyperons, the dependence on the charged component becomes larger and we thus expect more important Coulomb effects on the phase diagram. This is confirmed by the results, see Fig. 3, where the phase diagram is displayed in the plane n_B - n_L . As before, the arrows mark the directions of the order param-

eter. For the sake of completeness the phase coexistence domain of the simpler (n, p, Λ, e) -system is represented as a hatched yellow area. The qualitative structure of the phase diagram is similar to the case without electrons discussed before, see Fig. 2. It does not come as a surprise, however, that the phase coexistence region extends over a much smaller range in n_B , i.e. the phase transition region is quenched by Coulomb effects, in particular, for low n_L -values, where the the number of charged baryons participating in the phase transition is large. Compared with the case without electrons, the direction of phase separation is rotated in order to reduce the difference in $n_L = n_Q$ between the two phases. The reason is the large incompressibility of electrons, effectively suppressing electron density fluctuations. For matter in β -equilibrium, relevant for cold neutron stars, a large density domain is actually covered by phase coexistence, roughly between $0.3 \lesssim n_B \lesssim 0.43 \text{ fm}^{-3}$, see the dashed line in Fig. 3.

As easy to anticipate, for small values of μ_Q , corresponding to the largest n_L -values shown in the figure, where the Λ and Σ production thresholds are sufficiently different for the corresponding phase coexistence regions to be separated, the coexistence domain associated to the onset of Λ s in the complete system sits exactly on the top of that corresponding to the (n, p, Λ, e) -system. At smaller μ_L values, i.e. for small values of n_L , the two systems have different phase coexistence regions with the one of the full baryonic octet wider than that of the simpler mixture due to the participation of Σ -hyperons. In particular, in the left bottom part of Fig. 3 the low density boundary of the phase coexistence region of the (n, p, Y, e) -system is distinct from that corresponding to the (n, p, Λ, e) -mixture. There are two reasons for that. For the lowest considered n_L -values, the low density phase of the restricted system is purely nucleonic while, upon considering the full baryonic octet, the low density phase contains Σ^- , too, the first hyperons to appear in that case. At slightly higher but still low n_L -values, the discrepancy arises from the composition of the high density phase, which contains Σ -hyperons in addition to nucleons and Λ -hyperons.

It is important to stress that the phase diagram will obviously depend on the assumed coupling constants in all channels. For instance, if a repulsive potential is employed for Σ -hyperons, as suggested by the analyses of (π^-, K^+) -spectra, their threshold will be shifted to higher densities and the associated phase transition will consequently be shifted.

For the simpler $n, p, \Lambda+e$ -system, it has been shown that this phase transition persists in this model at finite temperature, with a phase separation direction almost independent of T [30]. Increasing the temperature, the width of the coexistence region, shown for $T = 0$ in Fig. 3, at low values of n_L shrinks, leading to the appearance of a critical point above some finite value of T of the order 15 MeV which survives up to very high temperature. It moves to higher n_L -values with increasing temperature, see Fig. 4, where the critical temperature and the corresponding electron fraction $Y_e = n_L/n_B$ are shown. Since the character of the phase transition remains “strangeness-driven”,

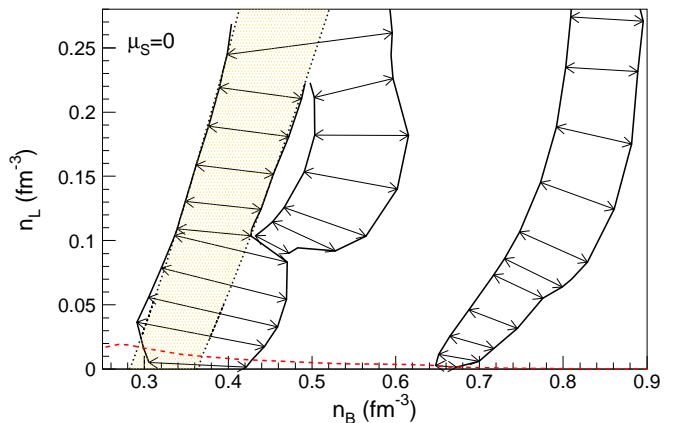


Fig. 3. (Color online) Phase diagram of the (n, p, Y, e) -system at $T=1$ MeV for $\mu_S = 0$ as provided by BGI parameterization [42] in the n_B - n_L -plane. The (red) dashed curve marks the path corresponding to β -equilibrium. The yellow hatched band marks the phase coexistence region obtained within the simpler (n, p, Λ, e) -system [30].

we do not expect any qualitative change upon including the full octet, with quantitative values of the same order. These values are typically reached within the cooling proto-neutron star, meaning that effects of criticality should be experienced if there is a strangeness-driven phase transition.

In particular, the neutrino mean free path, λ , due to scattering off baryons should be strongly influenced. In order to explore this point, we show calculations of the latter including the long-range correlations, essential for the study of criticality. The linear response approximation is employed. In addition, since we focus here on the impact of density fluctuations close to the critical point, where spin-density fluctuations are expected to be small [47, 48], only the vector channel will be considered. Then, in the non-relativistic limit for the baryonic components the mean free path at temperature T of a neutrino with initial energy E_ν is given by [49, 50],

$$\frac{1}{\lambda} = \frac{1}{\lambda^V(E_\nu, T)} = \frac{G_F^2}{16\pi^2} \int (1 + \cos\theta) \mathcal{S}^V(q, T) (1 - f_\nu(\mathbf{k}_3)) d\mathbf{k}_3. \quad (6)$$

G_F denotes here the Fermi constant, θ is the angle between the initial and final neutrino momentum ($=\mathbf{k}_3$), q is the transferred energy-momentum, $q = (\omega, \mathbf{q})$, and f_ν is the Fermi-Dirac distribution of the outgoing neutrino. \mathcal{S}^V represents the dynamical response function in the vector channel. It is defined as

$$\mathcal{S}^V(q, T) = -\frac{2}{\pi} \frac{1}{1 - \exp(-\omega/T)} \times (c_V^n \ c_V^p \ c_V^\Lambda) \Pi^V(q, T) \begin{pmatrix} c_V^n \\ c_V^p \\ c_V^\Lambda \end{pmatrix}, \quad (7)$$

where $\Pi^V(q, T)$ is the vector-polarization matrix for the three species n, p , and Λ . In mean field approximation it

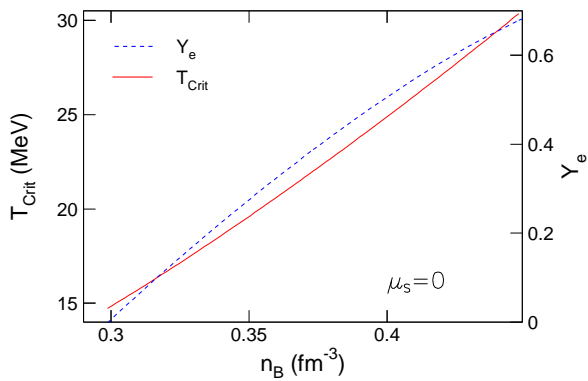


Fig. 4. (Color online) Electron fraction, Y_e , and n_B at the corresponding critical temperature for $\mu_S = 0$ within the (n, p, Λ, e) -system. Figure taken from Ref. [30].

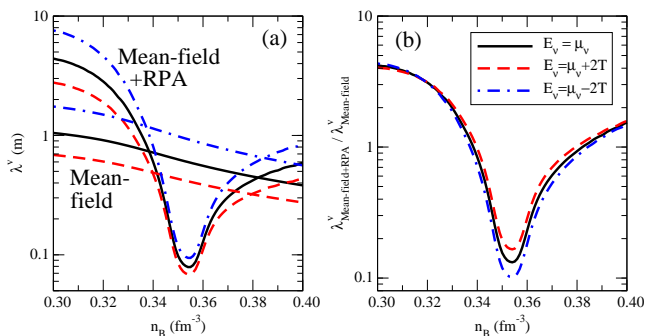


Fig. 5. (Color online) (a) Neutrino mean free path for the scattering off n , p , and Λ at $T = 20$ MeV along a constant- $Y_e = 0.2981$ trajectory in the phase diagram for $E_\nu = \mu_\nu$, $\mu_\nu \pm T$ as a function of the baryonic density, n_B . The result of the mean-field approximation is compared with a mean-field+RPA calculation. (b) The ratio of the mean free path within mean-field+RPA over mean-field approximation is shown. Figure taken from Ref. [30].

reduces to the Lindhard functions [51] and in mean-field + RPA approximation it is the solution of the Bethe-Salpeter equations [48, 49, 50]. The coupling constants, c_V^i , are $-1(n), 0.08(p), -1(\Lambda)$ [52]. The residual p-h interaction entering the calculation of the polarization matrix is closely related to the curvature matrix without electrons [53] and reflects therefore the criticality of the phase transition.

In Fig. 5 we show the calculation within the n, p, Λ, e -system⁴. The depletion of the mean-free path in the vicinity of the critical point is clearly visible. The possible impact of a phase transition on the hydrodynamics of core collapse will be discussed in Sec. 4.

3 Thermal effects on the EoS including non-nucleonic degrees of freedom

In heavy-ion collisions (HICs), core-collapse supernovae and neutron star or black-hole neutron star mergers, matter is strongly heated and thermal effects on the EoS become important. Of course, the conditions are very different in HICs compared with the astrophysical events. In particular, matter in HICs cannot be considered in strangeness changing weak equilibrium, but rather the zero net strangeness of the two colliding nuclei is conserved during the entire collision due to the very short timescales. However, thermal effects lead to a considerable production of non-nucleonic degrees of freedom, hyperons, nuclear resonances, strange and non-strange mesons, and in the early phase probably a quark-gluon plasma. This clearly shows the importance of thermal effects on the composition of matter. Therefore in compact star astrophysics, where in addition to being heated, matter is compressed to densities above nuclear matter saturation density, n_0 , non-nucleonic degrees of freedom are expected to occur, too.

This has been recognized shortly after the first discussions about hyperons and quarks in cold neutron stars, and EoSs have been developed to study the impact of additional particles, such as hyperons and mesons, as well as meson condensate and quark matter formation on the evolution of proto-neutron stars, see e.g. [54] for an early review. Inhomogeneous matter in the outer layers and the formation of the neutron star crust do not influence strongly the proto-neutron star evolution, such that in a first approximation it can be neglected. Therefore most of the works investigating thermal effects on the EoS, treat homogeneous matter at some given temperature or entropy per baryon and hadronic charge fraction, $Y_Q = n_Q/n_B$, with values relevant for proto-neutron star evolution, see e.g. [55, 56, 57, 58, 59, 60]. Only recently, some models have been proposed, including non-nucleonic degrees of freedom and treating the low-density and low-temperature inhomogeneous nuclear matter, too, see e.g. [20, 27, 61, 62].

Quark matter formation is very interesting in this context, in particular if the transition occurs during the early post-bounce phase, since then the related phase transition is visible in the supernova neutrino signal [27]. Such an early phase transition requires, however, a low transition density and therefore a relatively soft EoS which seems difficult to be reconciled with a maximum cold neutron star mass above $\sim 2M_\odot$ in agreement with recent observations [11, 12], see Ref. [63]. In the contracting and partially deleptonized proto-neutron star, higher densities and temperatures are reached, and the conditions are, therefore, more favorable for quark matter to appear. Such a transition could explain some gamma-ray-bursts or, via the scenario of so-called “quark-novae”, some unusual supernova light-curves, see the discussion in Ref. [64] and references therein. In addition, quark matter at not too high temperatures has a very rich phase structure related to different color superconducting phases with consequences for compact star phenomenology, for instance on neutron star cooling, see e.g. [65] for a review.

⁴ Electrons are not relevant for this calculation.

Here, we will concentrate on hadronic degrees of freedom, i.e. hyperons and mesons, and present some selected EoS in order to illustrate thermal effects on the appearance of these particles. Due to the computational complexity, only some microscopic calculations exist, see e.g. the BHF calculations of [66,67,68]. Most models employ phenomenological interactions, non-relativistic or relativistic mean field (RMF) ones. In the following section we will, therefore, briefly introduce the latter, the former has already been discussed in Sec. 2.2.

Pions, and to less extent kaons, have already been considered twenty years ago as possible candidates for the hot and dense matter in supernova cores and proto-neutron stars, see e.g. [55,56,69]. The authors of Ref. [69] argue that the temperature of the supernova core could be increased by the presence of pions. As a consequence, the number of electron neutrinos would increase resulting in a higher neutrino luminosity favoring a successful explosion. However, the employed pion-nucleon interaction is probably too attractive, and a more realistic interaction decreases the number of pions eventually present in supernova cores and thus the effect on the neutrino luminosity. For cold neutron stars, it is now commonly assumed that there is an s -wave πN repulsion, preventing pions from forming a Bose-Einstein condensate. Most recent works on the EoS for hot and dense matter neglect for simplicity any interaction and use a free pion gas [20,46,61,62]. This will be the case for the results shown below, too. At least for the high temperatures and low densities thermal effects should dominate and the interaction should be less important. Let us mention that in Ref. [61] it is shown that a parameterized s -wave πN repulsive interaction allows to avoid pion condensation at low temperatures but, since the effects of the interaction on the EoS are only important at low temperatures, and pionic effects are generally not the dominant contribution to the EoS, the model dependence of the results becomes very weak.

3.1 Relativistic mean field models for the EoS

The literature on phenomenological RMF models is large and many different versions exist (see e.g. [70]). The basic idea is that the interaction between baryons is mediated by meson fields. These are not real mesons, but introduced on a phenomenological basis with their quantum numbers in different interaction channels. Earlier models introduce non-linear self-couplings of the meson fields in order to reproduce correctly nuclear matter saturation and properties of nuclei, whereas more recently density-dependent couplings between baryons and the meson fields have been widely used. The Lagrangian of the model can be written in the following form

$$\begin{aligned} \mathcal{L} = & \sum_{j \in B} \bar{\psi}_j (i\gamma_\mu \partial^\mu - m_j + g_{\sigma j} \sigma + g_{\sigma^* j} \sigma^* \\ & + g_{\delta j} \boldsymbol{\delta} \cdot \mathbf{I}_j - g_{\omega j} \gamma_\mu \omega^\mu - g_{\phi j} \gamma_\mu \phi^\mu - g_{\rho j} \gamma_\mu \boldsymbol{\rho}^\mu \cdot \mathbf{I}_j) \psi_j \\ & + \frac{1}{2} (\partial_\mu \sigma \partial^\mu \sigma - m_\sigma^2 \sigma^2) - \frac{1}{3} g_2 \sigma^3 - \frac{1}{4} g_3 \sigma^4 \\ & + \frac{1}{2} (\partial_\mu \sigma^* \partial^\mu \sigma^* - m_{\sigma^*}^2 \sigma^{*2}) \\ & + \frac{1}{2} (\partial_\mu \boldsymbol{\delta} \partial^\mu \boldsymbol{\delta} - m_\delta^2 \boldsymbol{\delta}^2) \\ & - \frac{1}{4} W_{\mu\nu}^\dagger W^{\mu\nu} - \frac{1}{4} P_{\mu\nu}^\dagger P^{\mu\nu} - \frac{1}{4} \mathbf{R}_{\mu\nu}^\dagger \cdot \mathbf{R}^{\mu\nu} \\ & + \frac{1}{2} m_\omega^2 \omega_\mu \omega^\mu + \frac{1}{4} c_3 (\omega_\mu \omega^\mu)^2 \\ & + \frac{1}{2} m_\phi^2 \phi_\mu \phi^\mu + \frac{1}{2} m_\rho^2 \boldsymbol{\rho}_\mu \cdot \boldsymbol{\rho}^\mu, \end{aligned} \quad (8)$$

where ψ_j denotes the field of baryon j , and $W_{\mu\nu}, P_{\mu\nu}, \mathbf{R}_{\mu\nu}$ are the vector meson field tensors of the form

$$V^{\mu\nu} = \partial^\mu V^\nu - \partial^\nu V^\mu. \quad (9)$$

σ, σ^* are scalar-isoscalar meson fields, coupling to all baryons (σ) and to strange baryons (σ^*), respectively. $\boldsymbol{\delta}$ induces a scalar-isovector coupling.

In mean field approximation, the meson fields are replaced by their respective mean-field expectation values, which are given in uniform matter as

$$m_\sigma^2 \bar{\sigma} + g_2 \bar{\sigma}^2 + g_3 \bar{\sigma}^3 = \sum_{i \in B} g_{\sigma i} n_i^s \quad (10)$$

$$m_{\sigma^*}^2 \bar{\sigma}^* = \sum_{i \in B} g_{\sigma^* i} n_i^s \quad (11)$$

$$m_\delta^2 \bar{\delta} = \sum_{i \in B} g_{\delta i} t_{3i} n_i^s \quad (12)$$

$$m_\omega^2 \bar{\omega} + c_3 \bar{\omega}^3 = \sum_{i \in B} g_{\omega i} n_i \quad (13)$$

$$m_\phi^2 \bar{\phi} = \sum_{i \in B} g_{\phi i} n_i \quad (14)$$

$$m_\rho^2 \bar{\rho} = \sum_{i \in B} g_{\rho i} t_{3i} n_i, \quad (15)$$

where $\bar{\delta} = \langle \delta_3 \rangle$, $\bar{\rho} = \langle \rho_3^0 \rangle$, $\bar{\omega} = \langle \omega^0 \rangle$, $\bar{\phi} = \langle \phi^0 \rangle$, and t_{3i} represents the third component of isospin of baryon i with the convention that $t_{3p} = 1/2$. The scalar density of baryon i is given by

$$n_i^s = \langle \bar{\psi}_i \psi_i \rangle = \frac{1}{\pi^2} \int k^2 \frac{M_i^*}{\sqrt{k^2 + M_i^{*2}}} \{f[\epsilon_i(k)] + \bar{f}[\epsilon_i(k)]\} dk, \quad (16)$$

and the number density by

$$n_i = \langle \bar{\psi}_i \gamma^0 \psi_i \rangle = \frac{1}{\pi^2} \int k^2 (f(\epsilon_i(k)) - \bar{f}(\epsilon_i(k))) dk. \quad (17)$$

f and \bar{f} represent here the occupation numbers of the respective particle and antiparticle states with the single-particle energies, $\epsilon_i(k) = \sqrt{k^2 + M_i^{*2}}$, which reduce to a step function at zero temperature. The effective baryon mass M_i^* depends on the scalar mean fields as

$$M_i^* = M_i - g_{\sigma i} \bar{\sigma} - g_{\sigma^* i} \bar{\sigma}^* - g_{\delta i} t_{3i} \bar{\delta}, \quad (18)$$

and the effective chemical potentials, $(\mu_i^*)^2 = (M_i^*)^2 + k_{Fi}^2$, are related to the chemical potentials via

$$\mu_i^* = \mu_i - g_{\omega i} \bar{\omega} - g_{\rho i} t_{3i} \bar{\rho} - g_{\phi i} \bar{\phi} - \Sigma_0^R. \quad (19)$$

The rearrangement term

$$\Sigma_0^R = \sum_{j \in B} \left(\frac{\partial g_{\omega j}}{\partial n_j} \bar{\omega} n_j + t_{3j} \frac{\partial g_{\rho j}}{\partial n_j} \bar{\rho} n_j + \frac{\partial g_{\phi j}}{\partial n_j} \bar{\phi} n_j - \frac{\partial g_{\sigma j}}{\partial n_j} \bar{\sigma} n_j^s - \frac{\partial g_{\sigma^* j}}{\partial n_j} \bar{\sigma}^* n_j^s - t_{3j} \frac{\partial g_{\delta j}}{\partial n_j} \bar{\delta} n_j^s \right). \quad (20)$$

is present in density-dependent models to ensure thermodynamic consistency.

In the present paper we consider a set of models frequently used in the literature that succeed in describing a $2M_\odot$ neutron star. In particular, we will show results for three non-linear models, GM1 [71], TM1 [72] and TM1-2 [73], and two density-dependent ones, DDH δ [74,75] and DD2 [76]. For the GM1 parameterization, $c_3 = 0$, and the δ -field is absent in GM1, TM1, TM1-2 and DD2. The TM1-2 parametrization has properties similar to TM1 at saturation but is stiffer at large densities. TM1-2 has a quite large symmetry energy slope L at saturation ($L = 110$ MeV), therefore we have considered a modification with a smaller slope, $L = 55$ MeV, by including a $\omega\rho$ mixing term which allows us to discuss the influence of the density dependence of the symmetry energy on the results. In Table 2 we show two parametrizations for TM1-2 corresponding to the two values of L . The density-dependent models assume $g_2 = g_3 = c_3 = 0$ (no non-linear terms) and the couplings become density dependent,

$$g_i(n_B) = g_i(n_0) h_i(x), \quad x = n_B/n_0. \quad (21)$$

There exist different parameterization employing mostly the same functional forms. Within the DDH δ and the DD2 parameterization, the following forms are assumed for the isoscalar couplings,

$$h_i(x) = a_i \frac{1 + b_i(x + d_i)^2}{1 + c_i(x + d_i)^2} \quad (22)$$

and

$$h_i(x) = a_i \exp[-b_i(x - 1)] - c_i(x - d_i). \quad (23)$$

for the isovector ones. In the following we will show results for extensions of the STOS [3] and the statistical model EoS by Hempel and Schaffner-Bielich [6] (BHB model), that have as underlying parametrizations, respectively, TM1 and DD2, and for the non-relativistic EOS, LS220 [77]. As extra degrees of freedom pions, Λ -hyperons, or all hyperons of the baryonic octet have been considered, and accordingly, we will add the termination π , Λ or Y to the name of the EoS. The original references are given in Table 3, together with the hyperonic interaction employed.

The wealth of nuclear data allows to constrain reasonably the parameter values of the interaction between nucleons. The corresponding parameter values of the different models can be found in the above references and the resulting nuclear matter properties are listed in Table 2. In addition to standard properties of isospin symmetric nuclear matter, the energy per baryon of pure neutron

matter at saturation density is given, too, for which recently a range

$$14.1 \lesssim E/A(n_0) \lesssim 21.4 \text{ MeV}. \quad (24)$$

has been derived from microscopic calculations within chiral nuclear forces [78]. This quantity is particularly interesting for the EoS of compact stars, completing the information about symmetric matter, since very asymmetric matter close to pure neutron matter is encountered. Except for the DDH δ -model, for which the value is too low, the employed models lie within the indicated range. The symmetry energy E_{sym} and its slope, L , containing information about the isospin dependence of the EoS, too, are as well important in this respect. For instance, it is well known that the radius of compact stars is very sensitive to L [79,80,81]. The models considered here span a wide range of values of L , with some of them being at the upper end of possible values [82].

Hyperonic data are scarce and it is therefore very difficult to obtain information on the interaction parameters in the hyperonic sector. Many recent works, see e.g. [18, 23, 84], use a procedure inspired by the symmetries of the baryon octet to reduce the number of free parameters. The individual isoscalar vector meson-baryon couplings can then be expressed in terms of $g_{\omega N}$ and a few additional parameters, $\alpha, \theta, z = g_1/g_8$, see e.g. [85] for details, as follows

$$\begin{aligned} \frac{g_{\omega\Lambda}}{g_{\omega N}} &= \frac{1 - \frac{2z}{\sqrt{3}}(1 - \alpha) \tan \theta}{1 - \frac{z}{\sqrt{3}}(1 - 4\alpha) \tan \theta}, & \frac{g_{\phi\Lambda}}{g_{\omega N}} &= -\frac{\tan \theta + \frac{2z}{\sqrt{3}}(1 - \alpha)}{1 - \frac{z}{\sqrt{3}}(1 - 4\alpha) \tan \theta}, \\ \frac{g_{\omega\Sigma}}{g_{\omega N}} &= \frac{1 + \frac{2z}{\sqrt{3}}(1 - \alpha) \tan \theta}{1 - \frac{z}{\sqrt{3}}(1 - 4\alpha) \tan \theta}, & \frac{g_{\phi\Sigma}}{g_{\omega N}} &= \frac{-\tan \theta + \frac{2z}{\sqrt{3}}(1 - \alpha)}{1 - \frac{z}{\sqrt{3}}(1 - 4\alpha) \tan \theta}, \\ \frac{g_{\omega\Xi}}{g_{\omega N}} &= \frac{1 - \frac{z}{\sqrt{3}}(1 + 2\alpha) \tan \theta}{1 - \frac{z}{\sqrt{3}}(1 - 4\alpha) \tan \theta}, & \frac{g_{\phi\Xi}}{g_{\omega N}} &= -\frac{\tan \theta + \frac{z}{\sqrt{3}}(1 + 2\alpha)}{1 - \frac{z}{\sqrt{3}}(1 - 4\alpha) \tan \theta}, \\ \frac{g_{\phi N}}{g_{\omega N}} &= -\frac{\tan \theta + \frac{z}{\sqrt{3}}(1 - 4\alpha)}{1 - \frac{z}{\sqrt{3}}(1 - 4\alpha) \tan \theta}. \end{aligned} \quad (25)$$

The following values are commonly assumed: $\tan \theta = 1/\sqrt{2}$, corresponding to ideal ω - ϕ -mixing, $\alpha = 1$, and $z = 1/\sqrt{6}$. The latter value reflects an underlying $SU(6)$ -symmetry, and only recent studies in view of the observation of high mass neutron stars have relaxed this assumption, for example [18, 22, 61, 84], or even varied freely the hyperonic isoscalar vector couplings, see e.g. [26].

In the isovector sector, not the same procedure is applied, since this would lead to contradictions with the observed nuclear symmetry energy. $g_{\rho N}$ is therefore left as a free parameter, adjusted to the desired value of the symmetry energy, and the remaining isovector vector couplings are fixed by isospin symmetry.

For the scalar sector, different methods are applied. In Ref. [21] a symmetry inspired procedure is discussed together with the constraints imposed by hypernuclear data. In [83], the value of the $\sigma\Lambda$ -coupling is taken from a fit of the binding energies of single Λ -hypernuclei resulting in $R_{\sigma\Lambda} = 0.621$. In many other works, see e.g. Refs. [18, 23, 26, 61], the information from hypernuclear data on hyperonic single-particle mean field potentials is used to con-

	K [MeV]	E_{sym} [MeV]	n_0 [MeV]	B [MeV]	L [MeV]	$E/A(n_0)$ [MeV]
GM1	300	32.5	0.153	16.3	94	18.6
TM1	281	36.9	0.145	16.3	111	21.1
TM1-2	282	37.2	0.146	16.4	111/55	21.8/17.1
DD2	243	31.7	0.149	16.0	55	18.2
DDH δ	240	25.1	0.153	16.3	44	10.6
LS220	220	28.6	0.155	16.0	74	14.4

Table 2. Nuclear matter properties of the models considered in this study for symmetric nuclear matter at saturation, except for the last column where the energy per baryon of neutron matter at n_0 is given with the neutron mass subtracted.

Model	Nuclear interaction	$R_{\sigma^* \Lambda}$	$R_{\sigma^* \Xi}$	$R_{\sigma^* \Sigma}$	$R_{\omega Y}$	$R_{\phi Y}$	$U_{\Lambda}^{(\Lambda)}(n_0/5)$ [MeV]	$U_{\Xi}^{(\Xi)}(n_0/5)$ [MeV]	$U_{\Sigma}^{(\Sigma)}(n_0/5)$ [MeV]	Reference(s)
BHBA	DD2	0	-	-	1	0	-5	-	-	[23]
BHBA ϕ	DD2	0	-	-	1	1	7	-	-	[23]
STOSA	TM1	0	-	-	1	0	6	-	-	[83]
LS220A	LS220	-	-	-	-	-	-5	-	-	[30, 46]
STOSY	TM1	0.67	1.23	0.67	1	1	-11	-8	5	[61]
GM1 Y6	GM1	0	0.55	0	2	2	-7	-10	13	[26]
TM1-2 Y1	TM1-2(111)	0	0	0	1	1	1.7	21.1	16.2	[26]
TM1-2 Y2	TM1-2(55)	0	0	0	1	1	1.7	21.1	16.2	[26]
TM1-2 A4	TM1-2(111)	1.68	1.68	1.68	1.5	2	-41.1	36.0	-21	[26]
TM1-2 A6	TM1-2(55)	1.58	1.58	1.58	1.5	2	-33.7	44.4	-12.8	[26]
DDH δ Y4	DDH δ	1.03	0	0	1.5	0.85	-5	79	62	[26]
220g3	LS220	-	-	-	-	-	-2.73	-2.73	-2.73	[20]

Table 3. Summary of coupling parameters used within the different models. The nuclear interaction is indicated in the second column and those of hyperons in columns 3-7. The couplings to the isoscalar vector mesons are defined with respect to the respective $SU(6)$ values and the couplings to σ^* are defined with respect to $g_{\sigma N}$. The coupling parameters of the two non-relativistic models, LS220A and 220g3 are given in Table 1. In addition, the values of the hyperon single particle potentials in hyperon matter at $n_0/5$ are given for information. The last column indicates the reference(s) to the original work. The models in the upper part thereby consider only Λ -hyperons whereas those in the lower part allow all hyperons to have nonzero abundances.

strain the coupling constants. Let us emphasize that almost no information is available on the hyperon-hyperon (YY)-interaction apart from a few light double- Λ -hypernuclei, that constrain only the low density behavior. Therefore, the corresponding couplings, within the RMF models, in particular σ^* and ϕ are very poorly constrained. In most recent models ϕ -mesons are added in order to be compatible with the $2 M_{\odot}$ neutron star, whereas often σ^* is neglected (see e.g. [16, 18, 23]). This leads, however, to a very repulsive YY -interaction already at very low densities [26, 61, 86] which does not appear very realistic in view of the double- Λ -hypernuclear data. In Table 3 we summarize the coupling parameters used within the different models employed here. We list, in addition, the values of the corresponding hyperonic single particle potentials in hyperonic matter. Data on the bond energy of double- Λ -hypernuclei can be reinterpreted in terms of the Λ potential in Λ matter at the average density of Λ inside those nuclei [44, 87]. Mean-field calculations have shown that in light nuclei (from He to C) the average Λ density is close to one fifth of the saturation density [44, 87]. We have therefore chosen this density for the reference values of the hyperonic potentials.

The model LS220A presents a strangeness-driven phase transition at the onset of Λ -hyperons [29, 30], see Sec. 2.

Among the relativistic models, the parameter sets TM1-2A4/TM1-2A6 are chosen at the limit of presenting a thermodynamic instability at the onset of Λ -hyperons and stable with respect to all other hyperons [26]. The other models do not show any instability related to the onset of hyperons. To summarize, we believe that the large set of employed models and coupling constants gives a representative estimate of the present theoretical uncertainties in the high density equation of state modelling at finite temperature.

3.2 Hyperons and pions in the finite temperature EoS

Let us start with some comments on the EoS of cold β -equilibrated neutron stars including non-nucleonic degrees of freedom, for more details see [33]. By simple arguments based on the Pauli principle, for a system composed of fermionic particles, additional degrees of freedom tend to soften the EoS. In turn, this reduces the neutron star maximum mass, eventually being in contradiction with the recently observed masses [11, 12]. The way out is of course that the interaction must be much more repulsive at high density than presently assumed. This is true for hyperons and quarks. On the quark side, this leads to the problem

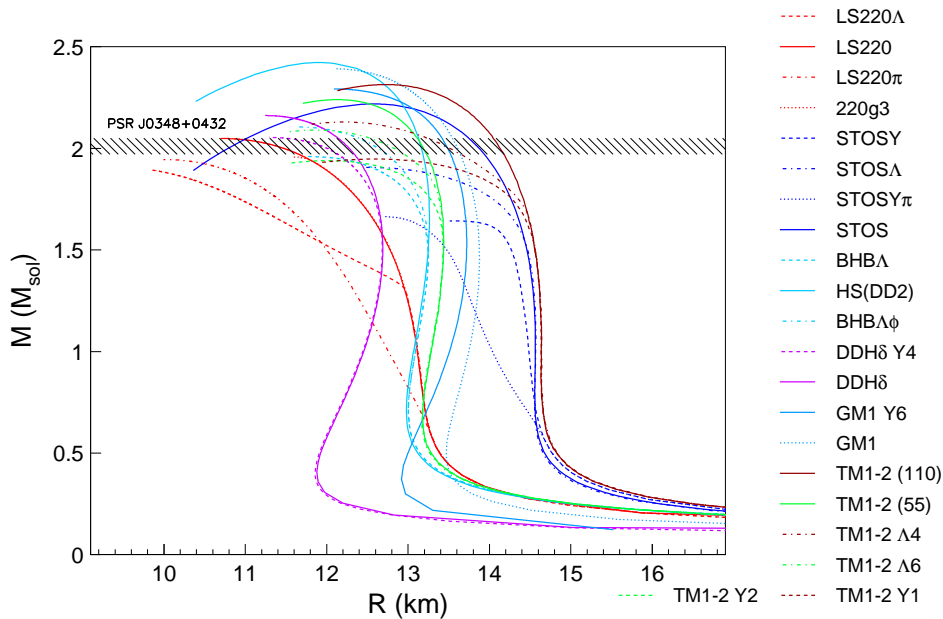


Fig. 6. (Color online) Mass-radius relation of a spherically symmetric cold β -equilibrated neutron star for different EoS including hyperons and/or pions and the corresponding purely nuclear EoS.

Model	M_{max} [M_{\odot}]	$R_{1.4}$ [km]	f_S	$n_B^{(c)}$ [fm $^{-3}$]
GM1	2.39	13.7	0	0.84
DD2	2.42	13.2	0	0.84
TM1 (STOS)	2.23	14.5	0	0.82
TM1-2(L=111)	2.31	14.3	0	0.81
TM1-2 (L=55)	2.24	13.3	0	0.86
DDH δ	2.16	12.6	0	0.98
LS220	2.06	12.7	0	1.11
GM1 Y6	2.29	13.8	0.04	0.85
BHB Λ	1.96	13.2	0.05	0.95
BHB $\Lambda\Phi$	2.11	13.2	0.05	0.95
STOS Λ	1.91	14.4	0.04	0.88
STOSY	1.65	14.4	0.07	0.67
STOSY π	1.66	13.6	0.05	0.81
TM1-2 Y1	1.95	14.6	0.15	0.86
TM1-2 Y2	1.94	13.4	0.12	0.91
TM1-2 Λ 4	2.13	14.6	0.16	0.90
TM1-2 Λ 6	2.09	13.4	0.11	0.92
DDH δ Y4	2.05	12.7	0.04	0.99
LS220 Λ	1.91	12.4	0.06	1.37
LS220 π	1.95	12.2	-	1.27
220g3	1.95	12.7	0.005	0.98

Table 4. Results calculated within different models at zero temperature: maximum mass of a cold spherical symmetric neutron star in β -equilibrium, radius at a fiducial mass of $M = 1.4M_{\odot}$, the total strangeness fraction, f_S , representing the integral of the strangeness fraction $Y_s/3$ over the whole star as in Ref. [18], and the central baryon number density. In the upper part purely nucleonic models are listed and in the lower part those containing hyperons and/or pions are given.

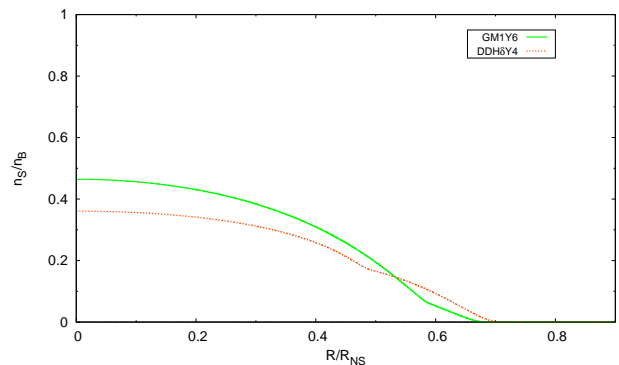


Fig. 7. (Color online) Strangeness fraction profiles of the maximum mass configurations within some of the EoS models shown in Fig. 6.

of reconfinement, i.e. the hadronic EoS becomes again energetically favored at some very high density [88], and on the hyperonic side the additional repulsion leads in general to a very low strangeness content of neutron stars [18], see [26] for models with higher strangeness content.

As observed in Ref. [89], another point is that in many models with hyperons compatible with the neutron star mass constraint, see e.g. [16,18], relatively large radii of about 14 km for a non-rotating spherical neutron star with the canonical mass of $1.4M_{\odot}$ are obtained, well above some recently suggested values, see e.g. [90]. Radius determinations are difficult and they are presently far from being as reliable as the mass observations from Refs. [12, 11]. The main problem is that the extraction of radii from observations is much more model-dependent and the low

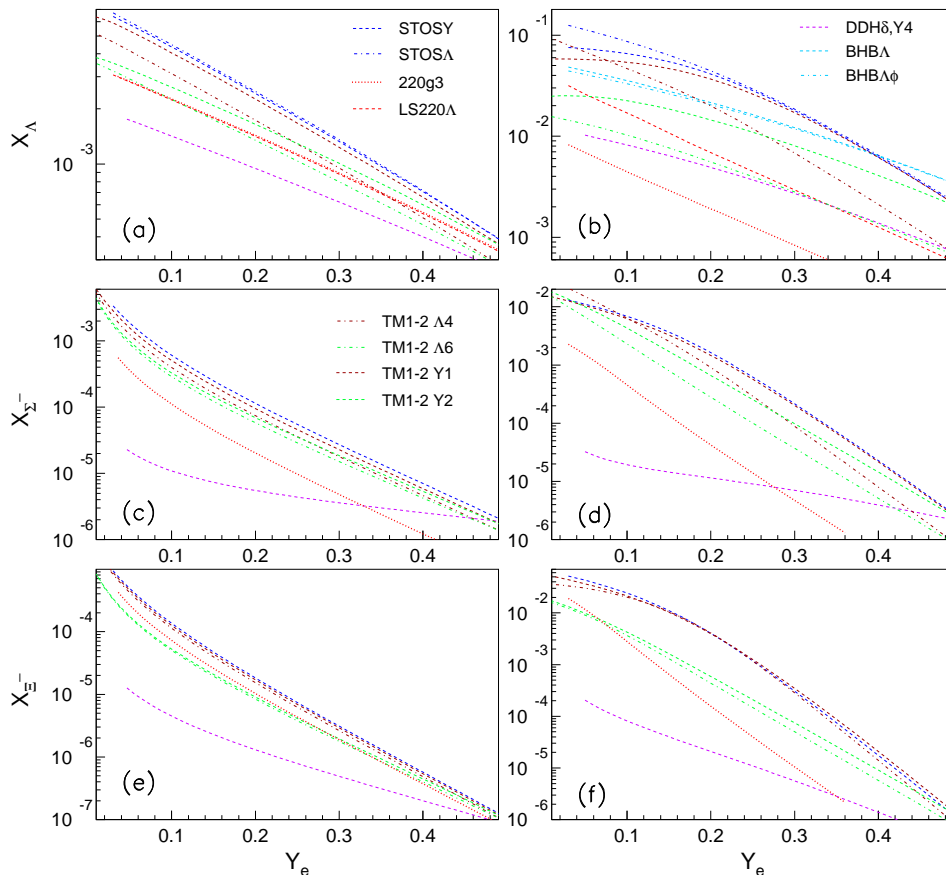


Fig. 8. (Color online) Fractions of different hyperons as a function of the electron fraction at a temperature of 25 MeV and for $n_B = 0.15 \text{ fm}^{-3}$ (left) and $n_B = 0.3 \text{ fm}^{-3}$ (right) corresponding roughly to once and twice nuclear matter saturation density. The fractions of $\Sigma^{0,+}$, Ξ^0 are not shown since they are always much smaller.

radii are not uncontested. A summary and discussion of different observational radius determinations can be found e.g. in Ref. [89]. Anyway, concerning hyperons in neutron stars, there are some examples with lower radii [15, 21, 23, 26].

Following the above remarks, we have chosen for our discussion of thermal effects different models with very different behavior for cold β -equilibrated neutron stars. As can be seen from Fig. 6, where the mass-radius relations for a non-rotating spherically symmetric neutron star are shown, the obtained range in radii for intermediate masses is relatively large. The onset of the additional degrees of freedom is clearly visible in the different curves as an evident change in the slope. In the models where only hyperons as non-nucleonic degrees of freedom are present, the radius at a gravitational mass of $M = 1.4M_\odot$ is mainly determined by the nuclear part of the EoS, thus strongly influenced by the parameter L , see Table 2, since hyperons appear only at densities above the central densities of these stars. If pions are included, on the other hand, they show up already at roughly saturation density and lower the radii already for neutron stars with masses below $1.4M_\odot$. A solution in order to obtain lower radii could thus be that a mesonic contribution should not be neglected. We should, however, be careful with a definite conclusion

here, since the models for including pions shown here are very crude, see above, and the pion-nucleon interaction is neglected.

Depending on the hyperonic interaction chosen, the models give very different maximum masses – not all are compatible with the recent constraints – and the strangeness content, see the examples shown in Fig. 7, covers a wide range, too. A summary of the zero temperature results can be found in Table 4. Concerning the EoS with non-nucleonic degrees of freedom, which have been extended to finite temperature, there are only a few which are compatible with the $2M_\odot$ constraint, see e.g. [59]. In particular, the existing EoS covering the whole range of temperature, electron fraction and density relevant for core-collapse supernovae and binary mergers either contain only Λ -hyperons [23, 30, 46, 83] or maximum cold neutron star masses well below $2M_\odot$ are obtained [61]. Here we will show first results extending the models of Ref. [26], compatible with existing constraints, to finite temperature and matter not necessarily in β -equilibrium, i.e. for different electron fractions, $Y_e = (n_{e^-} - n_{e^+})/n_B$.

As we will see, thermal effects favor the appearance of additional particles and with increasing temperature the effect of the interactions becomes less important. The reason is that the purely kinetic thermal part dominates if the

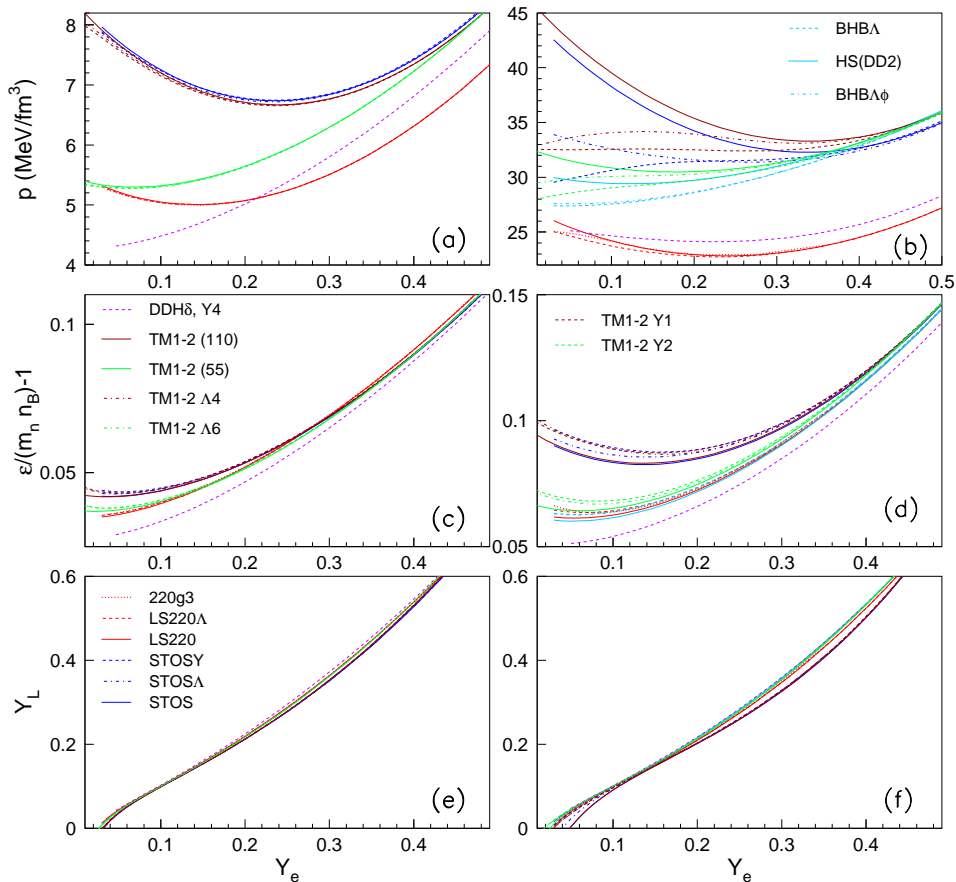


Fig. 9. (Color online) Thermodynamic quantities as functions of electron fraction $Y_e = Y_Q$ for a temperature $T = 25$ MeV and a baryon number density of $n_B = 0.15 \text{ fm}^{-3}$ (left) and $n_B = 0.3 \text{ fm}^{-3}$ (right). The upper panels show the pressure, the middle ones the internal energy per baryon with respect to the neutron mass and the lower ones the electron lepton fraction $Y_L = Y_e + Y_{\nu^e}$ under the assumption of β -equilibrium. No neutrinos are included in pressure and energy.

density does not become too high. Let us stress that all the models we are showing here are based on phenomenological models with parameters fixed to zero temperature properties of nuclear matter, nuclei, nucleons and other hadrons. It could be that these effective couplings depend on temperature, although there are indications that this is not the case. In Ref. [91] a RMF-model is compared with finite temperature microscopic Dirac-Brueckner-Hartree-Fock calculations, showing the thermal modifications of the effective couplings is almost negligible. Similar conclusions are obtained with non-relativistic phenomenological Skyrme type models [92,93].

In Fig. 8 the fractions $X_i = n_i/n_B$ of Λ , Σ^- and Ξ^- are shown as a function of the electron fraction which equals the hadronic charge fraction for a constant temperature of $T = 25$ MeV and two baryon number densities: $n_B = 0.15 \text{ fm}^{-3}$ (left) and 0.3 fm^{-3} (right). This value of the temperature has been chosen since it corresponds in all present models to an entropy per baryon s_B between 1 and $3 k_B$, values which are often cited as typical conditions for proto-neutron stars, see e.g. [54,59,94]. Other hyperonic particle fractions are not shown since they are much lower. The temperature is still low compared with the chemical potentials, so that the abundances are dominated by the

latter. However, for the lower density, the temperature explains the appearance of the hyperons, which at zero temperature would not be present in matter. Therefore, the large negative charge chemical potential in matter with low charge fractions favors negatively charged particles resulting in very low abundances for the neutral and positively charged hyperons, except for the Λ -hyperons. Here, the lower mass compared with Σ -hyperons and Cascades compensates the effect of the charge chemical potential.

All hyperonic fractions decrease with increasing Y_Q . The reason is that not only the charge chemical potential increases, but at the same time the baryon number chemical potential decreases due to the fact that the total baryon number remains constant: the proton fraction is larger, and nuclear matter becomes more symmetric for Y_Q close to 0.5, and, therefore the onset of hyperons is not favored. The effect is more pronounced for the charged particles than for the neutral Λ due to the effect of μ_Q . Qualitatively, all models show a similar behavior. The quantitative differences due to the different interactions are obviously more pronounced at higher density (right panel), than at lower density (left panel) where temperature is playing a larger role. We may also see how the hyperon fractions are sensitive to the density dependence

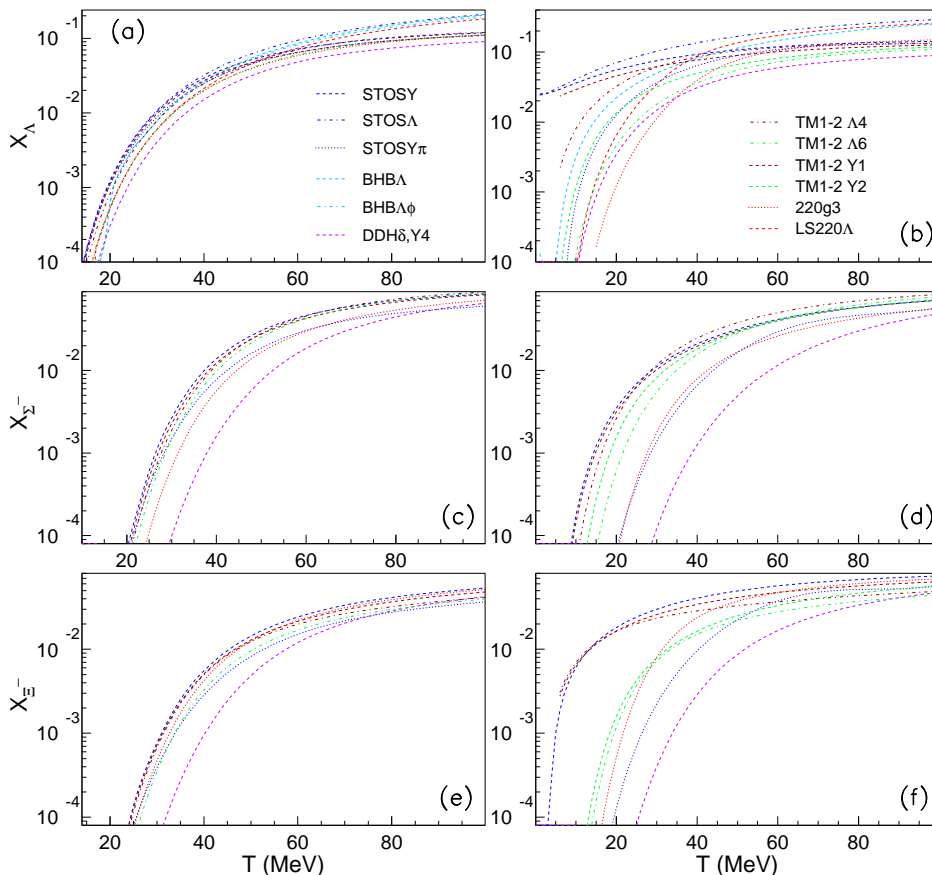


Fig. 10. (Color online) Same as Fig. 8 but as a function of temperature for an electron fraction $Y_e = 0.1$ and for $n_B = 0.15 \text{ fm}^{-3}$ (left) and $n_B = 0.3 \text{ fm}^{-3}$ (right).

of the symmetry energy: a softer symmetry energy favors the nucleonic degrees of freedom and the hyperon fractions are smaller. This is clearly seen comparing TM1-2 Y1 and Y2, Y1 having a harder symmetry energy and favoring larger fractions of hyperons. This effect is more visible for $n_B = 0.3 \text{ fm}^{-3}$ (right panels), where the temperature has a less important role.

No imprint of the strangeness-driven phase transition, see Sec. 2, is visible in the presented curves for LS220 Λ or TM1-2 $\Lambda4/6$. The reason is that the critical density lies above $n_B = 0.3 \text{ fm}^{-3}$, the highest density shown here.

In Fig. 9 the pressure, the internal energy with respect to the neutron mass and the total lepton fraction under the assumption of β -equilibrium are shown within different EoS models. Comparing the purely nuclear models (solid lines) with their counterparts containing additional particles, it is evident that for given densities and a fixed temperature, the pressure is lowered by the additional particles. As can be seen by comparing STOS Λ with STOSY, the more degrees of freedom present, the lower the pressure. The two curves start to show a difference upon onset of other hyperons than Λ -hyperons.

At a temperature of 25 MeV, the abundances of the additional particles are still low, see above, such that the effect is not very pronounced. The difference in pressure in-

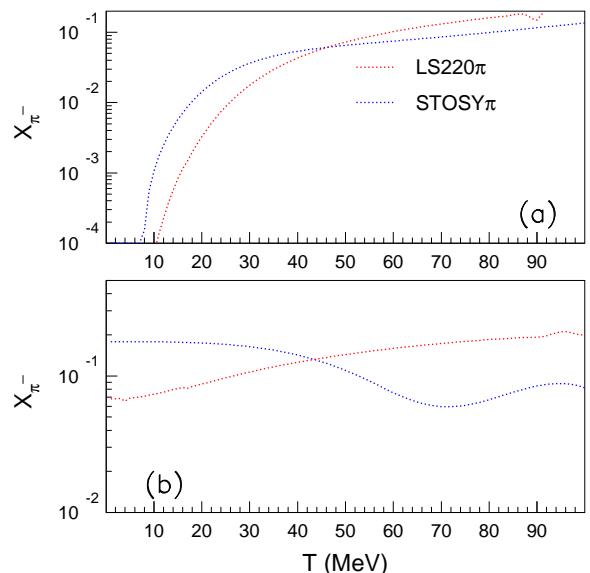


Fig. 11. (Color online) Same as Fig. 10, showing X_{π}^{-} within the models where they are present at $n_B = 0.15 \text{ fm}^{-3}$ (upper panel) and $n_B = 0.3 \text{ fm}^{-3}$ (lower panel).

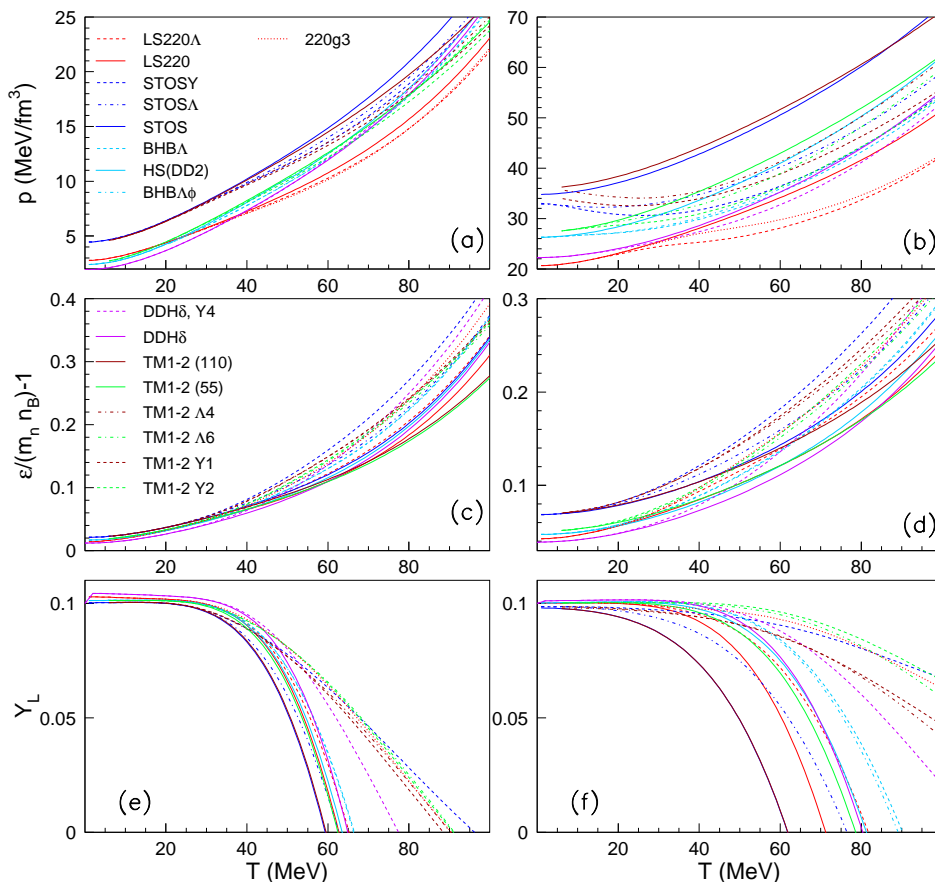


Fig. 12. Same as Fig. 9 but as function of temperature for an electron fraction $Y_e = Y_Q = 0.1$.

creases with decreasing Y_e since the abundances increase. Already at saturation density, due to thermal effects, there is a small reduction in pressure, but the effect becomes obviously stronger with increasing pressure. At twice nuclear matter saturation density there are still no hyperons in the zero temperature EoS, but thermal effects induce a clear effect on the EoS. Comparing the different hyperonic interaction models, in particular the different versions based on TM1-2, it can be seen that the interaction plays some role in determining the pressure.

In the middle panels, the internal energy defined as

$$\epsilon = \frac{\varepsilon}{n_B m_n} - 1, \quad (26)$$

with ε denoting the total energy density, is displayed. In contrast to the pressure, which is decreased for given densities and temperatures if hyperons are included, it is – slightly for the conditions shown in Fig. 9 – increased due to the presence of hyperons. This is understandable since hyperons are more massive than nucleons, thus for a given baryon number density, if a nucleon is replaced by a hyperon, the energy density is increased.

In the lower panels, the total electron lepton fraction is shown, $Y_L = Y_e + Y_{\nu^e}$, assuming β -equilibrium with neutrinos. This means that the neutrinos follow a Fermi-Dirac distribution with a chemical potential equal to the

electron lepton number chemical potential. The latter can be calculated as

$$\mu_{\nu^e} = \mu_L = \mu_e + \mu_Q = \mu_e + \mu_p - \mu_n, \quad (27)$$

with the electron chemical potential μ_e and the charge chemical potential μ_Q , given by the difference of proton and neutron chemical potentials. The neutrino chemical potential is increasing with increasing Y_e , such that in all models the neutrino fraction increases with Y_e . At this temperature only very small differences can be observed comparing the purely nucleonic models with the models including non-nucleonic degrees of freedom. Only at very low Y_e , a slightly higher Y_L is obtained within the latter models. s_B of $1 \sim 2 k_B$ together with trapped neutrinos and a value $Y_L = 0.4$ are typical values inside a proto-neutron star, see for instance Ref. [54]. In all the models shown here this would correspond to charge fractions between 0.3 and 0.4 with no appreciable difference between the nucleonic models and the others.

Depending on the progenitor, in the early post-bounce phase of a core-collapse event, much higher temperatures can be reached, of up to 100 MeV, see e.g. [46,95,96]. Therefore, in Fig. 10, the hyperonic particle fractions are displayed as function of temperature, again for $n_B = 0.15$ (left) and $n_B = 0.3 \text{ fm}^{-3}$ (right) and in Fig. 12 the corresponding pressure, internal energy and Y_L . The electron

fraction has been fixed to a low value of $Y_e = 0.1$. As discussed before, the hyperonic abundances become smaller for larger value of Y_e and typical values in the hot newly formed proto-neutron star are more of the order 0.3, while the neutrino free mean path is small and neutrinos are trapped inside the star. We have nevertheless chosen this low value to maximize the impact of non-nucleonic degrees of freedom, it corresponds to a scenario when the star becomes transparent to neutrinos.

In the upper panels of Fig. 10 the Λ -, in the middle panels the Σ^- - and in the lowest panels the Ξ^- -fractions are shown. They obviously increase all with temperature and X_Λ can reach more than 20 % at 100 MeV even at saturation density. At saturation density, all hyperons start to show up at roughly 25 MeV, independently of the model, whereas at $n_B = 0.3 \text{ fm}^{-3}$, differences are visible and in some models, Λ -hyperons exist already at very low temperatures.

The models allowing only Λ -hyperon states to be populated have considerably higher X_Λ than those including the whole baryon octet. The reason is simply, since the baryon number density is fixed, if other hyperons appear, they replace the Λ 's. Indeed, adding up all the hyperon fractions, the total strangeness fraction is similar within all models shown here. Again, as expected, the interaction dependence is more pronounced at higher density. The Ξ^- and Σ^- abundance in the DDH δ -model is probably much lower than in all other models due to the very strong YY -repulsion in these channels for the given parameterization, see Table 3. Again, the role of the symmetry energy becomes clear comparing the Σ^- and Ξ^- fractions of TM1-2 Y1 and Y2: for the harder symmetry energy the onset of hyperons occurs at smaller temperatures.

In Fig. 11, the fractions of π^- are shown within the two models considered here which contain pions. π^0 and π^+ have much lower abundances, the fractions stay below 1% except above 80 MeV and are therefore not shown. At $n_B = 0.15 \text{ fm}^{-3}$, i.e. roughly saturation density, the π^- -fraction exceeds 1% at about 25 MeV and increases up to about 20%. At twice this density, the fraction is less temperature dependent and remains between 5 and 15%. Despite this non-negligible abundances, the impact on the EoS is less important than for hyperons, see below.

At which temperature do the non-nucleonic particles start to considerably influence the EoS? In order to answer this question we display in Fig. 12 the pressure and the internal energy as function of temperature for the same Y_e and n_B as before. They clearly show the impact of the appearance of non-nucleonic degrees of freedom. The softening due to the additional degrees of freedom is again visible in the pressure and the internal energy is increased upon their onset. Again, at $n_B = 0.15 \text{ fm}^{-3}$, the particle content of the EoS has more influence on the behavior of the thermodynamic quantities than the details of the interaction, whereas, at twice this density, the different parameterizations result in different values for pressure and internal energy.

Concerning the lepton fraction assuming β -equilibrium displayed in the lower panels, in the EoS with non-nucleonic

degrees of freedom systematically higher values are obtained. The reason is that the presence of additional particles increases the charge chemical potential. The strong drop in Y_L occurs at higher temperatures, too. The reason for this drop is that the neutrino chemical potential is decreasing with increasing temperature in all models, much stronger in the purely nucleonic models due to the lower μ_Q than in the others.

Another interesting point about including non-nucleonic degrees of freedom is the fact that for a given entropy per baryon and electron fraction the temperature is significantly lower within an EoS including hyperons and/or pions than in a purely nuclear one, see e.g. [94]. This can be observed from Fig. 13, where for a fixed entropy per baryon, $s_B = 2k_B$, and constant electron fraction $Y_e = Y_Q = 0.1$ the temperature is shown as a function of baryon number density within different EoS used within this paper. Upon the onset of the additional degrees of freedom, i.e. about saturation density if pions are included and at a slightly higher density if only hyperons are allowed, the temperature curves considerably deviate from the purely nuclear EoS and increase much less stringently with density. As pointed out before, a softer symmetry energy gives rise to smaller hyperon fractions, and, as a consequence the temperature increases faster with density for a fixed entropy per baryon. The more degrees of freedom included, the lower the temperature. This can be understood looking at the temperature of a multicomponent Fermi gas at fixed entropy. For degenerate Fermi particles, i.e. for low temperatures compared to the Fermi energies of the system components, it is given by [97]

$$T \sim \frac{s}{\pi^2} \left(\frac{\sum_i p_{F_i}^3}{\sum_i p_{F_i} \sqrt{p_{F_i}^2 + (m_i^*)^2}} \right), \quad (28)$$

where p_{F_i} and $M_{F_i}^*$ are, respectively, the Fermi momentum of component i and corresponding effective mass, and s is the entropy per particle of the system. It is obvious that, increasing the number of degrees of freedom makes the temperature increase more slowly because the Fermi momenta of the system components decrease. This is a trivial thermodynamic effect: the appearance of hyperonic species implies that the energy is shared among an increased number of degrees of freedom, with consequently reduced thermal excitations for each of them.

This qualitative result does not depend very much on the value of Y_e and is confirmed for trapped neutrinos, too [94]. Assuming that in the region enclosed by the shock at early post-bounce times, the entropy profile is only weakly dependent on the EoS, this would mean that the non-nucleonic degrees freedom considerably lower the temperature with obviously important consequences for the neutrino distribution and the neutrino heating mechanism. The authors of Ref. [69] argue, however, that the presence of negatively charged particles other than electrons lowers the net electron number, releasing the electron degeneracy energy and resulting finally in a higher temperature of the supernova core. Without performing realistic simulations, including neutrino transport to de-

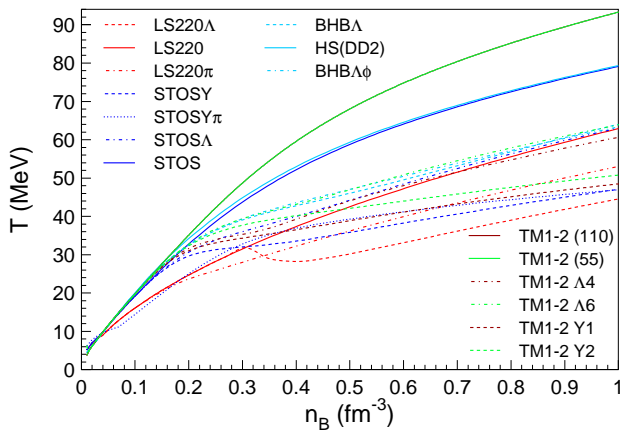


Fig. 13. (Color online) Temperature as a function of baryon number density at constant entropy per baryon $s = 2k_B$ and constant $Y_Q = 0.1$. Models including hyperonic degrees of freedom are compared with their purely nucleonic counterparts.

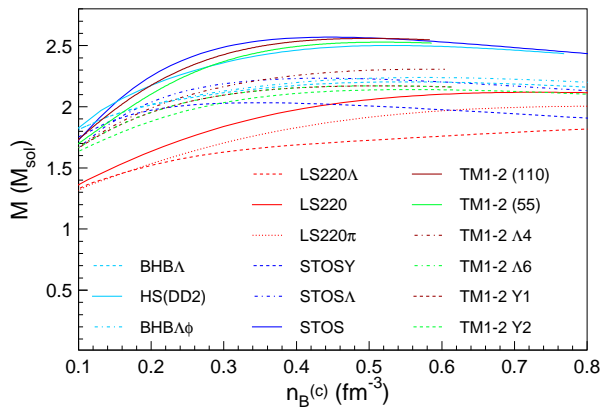


Fig. 14. Mass-central baryon density relations for isentropic spherical stars with $s = 4$ in neutrino-less β -equilibrium employing different EoS discussed in the text.

termine the electron fraction of the EoS, this question cannot be definitely answered.

Non-nucleonic degrees of freedom impact the maximum mass of a hot proto-neutron star, too. In general, compared with the cold β -equilibrated neutron star maximum mass, it is generally found that at typical early proto-neutron star conditions of $s_B = 2k_B$ and a fixed lepton fraction, $Y_L = 0.4$, the maximum mass is increased for all EoS [54,98]. Thermal effects are, however, at this entropy value less important than the effect of trapped neutrinos which induce a shift to higher Y_Q with respect to the cold neutrino-less β -equilibrium case. Indeed, inspecting the upper panels of Figs. 9 and 12, the pressure is more strongly influenced by a shift of $Y_e \sim 0.1$ to ~ 0.3 than between zero temperature and roughly 25 MeV for all EoS shown there. An exception are the EoS with a kaonic BEC considered in Ref. [55,56].

Since the abundances of hyperons and pions increase with decreasing $Y_e = Y_Q$, during the deleptonisation of the hot proto-neutron star the softening of the EoS with

Model	$M_{max}^{s=4}$	f_S	$n_B^{(c)}$	T_{max}
	M_\odot			
DD2	2.50	0	0.53	118
TM1 (STOS)	2.57	0	0.45	109
TM1-2(L=111)	2.56	0	0.50	104
TM1-2 (L=55)	2.53	0	0.52	109
LS220	2.12	0	0.74	123
BHBΛ	2.20	0.15	0.56	105
BHBΛφ	2.24	0.14	0.57	104
STOSΛ	2.23	0.13	0.43	72
STOSY	2.06	0.15	0.41	75
TM1-2 Y1	2.17	0.15	0.51	84
TM1-2 Y2	2.14	0.16	0.56	89
TM1-2 Λ4	2.31	0.18	0.58	95
TM1-2 Λ6	2.30	0.16	0.60	99
LS220Λ	1.85	0.15	1.06	122
LS220π	2.00	-	0.83	108

Table 5. Results calculated within different models: maximum mass of an isentropic star with entropy per baryon $s_B = 4k_B$ in β -equilibrium without neutrinos. Several quantities are listed for the maximum mass configuration: (a) The total strangeness fraction, f_S , representing the integral of the strangeness fraction $Y_s/3$ over the whole star as in Ref. [18], (b) The central baryon number density (c) The highest temperature reached. In the upper part purely nucleonic models are listed and in the lower part those containing hyperons and/or pions are given.

respect to the purely nucleonic one due to the additional degrees of freedom becomes more pronounced, see Fig. 9. This could give rise to metastable lepton-rich proto-neutron stars, see e.g. [54,55,68,99,100,101], and Sec. 4.2, too.

4 Impact of additional particles in astrophysical applications

Since we are mainly interested in thermal effects on an EoS not necessarily in β -equilibrium, we will, within this section, not consider any impact of hyperons or pions on properties of old and cold neutron stars, neither consider their cooling process. These points will be discussed elsewhere within this volume. As already mentioned earlier, the two systems predestinated to be influenced by the presence of non-nucleonic degrees of freedom are compact star binary mergers, neutron star-neutron star (NS-NS) and neutron star-black hole (NS-BH) mergers as well as BH formation in a core collapse supernova and the early post-bounce proto-neutron star evolution. Under some conditions, in particular –as mentioned earlier– a very soft EoS not compatible with a $2 M_\odot$ neutron star [63], the dynamics of an exploding supernova could be influenced, too: In Ref. [27] it has been shown that a phase transition to quark matter in the early post-bounce phase could induce a second shock wave, helping the supernova to explode. In general, densities and temperatures are, however, not high enough for non-nucleonic degrees of freedom to be considerably populated and to have a noteworthy impact

on an exploding supernova. We will therefore not discuss this scenario further here.

Since, despite recent efforts, only a few EoS with hyperons and/or pions are presently available covering the full range of thermodynamic variables necessary to perform realistic simulations of the above cited events, this field is under current development and we only want to give some hints on interesting results here.

4.1 Binary mergers

Coalescing relativistic binary systems containing compact objects, either NSs or black holes, receive a great interest since they are important sources of gravitational waves (GW), potentially detectable with next generation detectors such as advanced LIGO/VIRGO or KAGRA. In addition, they are believed to produce short gamma-ray bursts and they may represent a major source of heavy r-process elements. For more details, see e.g. the reviews [102, 103, 104].

The most promising track to obtain information on the EoS at high densities, i.e. containing potentially non-nucleonic degrees of freedom, is the post-merger phase. If the EoS supports the formation of a hypermassive neutron star, the frequencies of its normal modes are sensitive to the EoS and visible in the GW signal. The measurements of their frequencies could tightly constrain NS masses and radii since they are strongly correlated. It could even be possible to give an estimate for the NS maximum mass [105, 106, 107, 108, 109].

Other possibilities to constrain the EoS are the GW signal from the late inspiral, where the tidal deformation depends on the EoS [103, 104, 110] or the sGRB rate which depends on the maximum mass supported by the merger remnant [111, 112]. r-process nucleosynthesis depends critically on the EoS and matter composition [113, 114], too.

4.2 Black hole formation

It is well established that a massive star, after having consumed all its fuel, becomes gravitationally unstable, leading to a so-called core-collapse event. The iron core of the progenitor star collapses, bouncing back if the central density reaches roughly nuclear matter saturation density due to the stiffening of the EoS related to nuclear forces. A shock is formed, propagating outwards and at the center remains a hot lepton rich proto-neutron star. The following evolution is less well understood, see e.g. [115] for a detailed review. If the ejected material is successfully unbound after bounce, a neutron star is formed in a supernova explosion. If, however, the expanding shock is not able to break through the infalling material, the accretion pushes the proto-neutron star over its maximum mass which subsequently collapses to a black hole (BH). Due to larger accretion rates, such failed supernovae reach higher densities and temperatures than their exploding counterparts, which makes them an interesting tool to explore the EoS at high temperatures and supra-saturation densities.

Alternatively to this BH formation scenario in a failed supernova during the first second after bounce, a BH could equally well be formed at later times in the so-called delayed formation process, either because the proto-neutron star becomes unstable or because ejected material falls back and causes the collapse to a black hole.

Independently of the detailed scenario, the time until BH formation turns out to be sensitive to the underlying EoS. In spherical simulations, see e.g. [116, 117], the neutrino emission is abruptly stopped upon BH formation with a clear imprint in the observable neutrino signal. The time until BH formation, however, not only depends on the EoS, but on other factors, too, such as for instance the structure of the progenitor star or the rotation rate [118] such that the interpretation of such a signal would not be free of ambiguities although it presents a promising track to learn about the EoS of hot and dense matter.

Let us start now the discussion with the delayed BH formation. We have already mentioned that the hot proto-neutron star with trapped neutrinos is lepton rich and that hyperons and/or pions are less abundant than in cold neutron stars with very low Y_e . The same is true for EoS with a kaon condensed phase or with a transition to quark matter [98, 55, 56, 116, 99]. Thus imagine that we start from a proto-neutron star with few non-nucleonic degrees of freedom and a baryon mass above the maximum mass of a cold neutron star with these degrees of freedom. During cooling the proto-neutron star deleptonizes, and more and more additional particle states are populated until eventually the star exceeds its mass-limit and collapses to a BH, see e.g. [116, 119, 120].

Recently, some simulations of BH formation in failed supernovae have been performed employing EoS with pions and hyperons [46, 61, 95, 96, 121] or pions and quarks [122, 123]. All simulations show that the time until BH formation is sensitive to the underlying EoS and that the softening due to the additional degrees of freedom, be it hyperons, pions or quarks, considerably shortens the time until collapse to a BH. Since additional particles appear only deep inside the proto-neutron star, the neutrino signal is changed mainly by the duration of the signal compared with a purely nuclear EoS, see e.g. the detailed comparison in Ref. [96]. This could be different if the onset of the additional particles are accompanied by a phase transition, be it hyperons as in the LS220A EoS [46] or quarks [122, 123]. A phase transition sufficiently modifies the dynamics to induce an observable difference in the neutrino signal. In this context, Ref. [124] discusses the possibility that the QCD critical point could be reached in BH formation of core collapse.

An interesting correlation concerning the time until BH in a failed supernova has been raised in Refs. [125, 126]. They performed core-collapse simulations with a set of purely nuclear EoS starting from a $40 M_\odot$ progenitor with solar metallicity. They observed that the maximum mass of an isentropic proto-neutron star at $s_B = 4k_B$ in neutrino-less β -equilibrium can be correlated with the time until BH formation. In Fig. 14 we display the gravitational mass of such a proto-neutron star as func-

tion of the central density for a set of different EoS discussed within this paper. In Table 5 in addition to the corresponding maximum mass, the central baryon number density, the highest temperature reached and the integrated strangeness content of the different models are given. It is obvious that the maximum mass varies drastically between different EoS and shows in particular a strong reduction for the hyperonic EoS with respect to the purely nuclear ones. This can be understood since rather high temperatures are reached and the strangeness content of these proto-neutron stars is very high. Therefore, if the correlation with the time until BH formation is confirmed within a larger set of different EoS containing non-nucleonic degrees of freedom, too, then it could become a very interesting tool to constrain thermal properties of the EoS.

5 Summary and Conclusion

Within this paper we have discussed the appearance of non-nucleonic degrees of freedom in dense and hot matter relevant for the description of neutron stars, compact binary mergers and core-collapse supernovae. These non-nucleonic degrees of freedom could, thereby, be hadronic, i.e. hyperons or mesons or nuclear resonances, or quarks. We have put the emphasis on hyperons and mesons and discussed mainly two aspects.

The opening of hyperonic degrees of freedom in dense matter could happen smoothly or could be accompanied by a phase transition with a considerable effect on the thermodynamics and the hydrodynamical evolution of the system. We have presented here a complete study of the low temperature phase diagram including the entire baryon octet within the phenomenological non-relativistic Balberg and Gal model [42]. We have shown that the different hyperonic thresholds may be associated with thermodynamic instabilities, leading to first order phase transitions. These transitions can merge into a wide coexistence zone if the production thresholds of different hyperonic species are sufficiently close. As a consequence, a huge part of the phase diagram might correspond to phase coexistence between low-strangeness and high-strangeness phases. In contrast to the nuclear liquid-gas phase transition which is strongly quenched, this result is only slightly affected by Coulomb effects upon adding electrons and positrons to fulfill the charge neutrality constraint. As well as the phase transition to quark matter [27], this phase transition could affect the dynamics of core collapse [46]. In addition, at finite temperature a critical point associated with this strangeness-driven phase transition shows up, which might have sizable implications for the neutrino propagation in core-collapse supernovae.

There exist plenty of EoS models for cold neutron stars discussing the composition in the core and the possible appearance of hyperons, mesons, nuclear resonances or quarks. This does not hold for matter at finite temperature, where much less models exist, in particular if EoS models are excluded whose cold β -equilibrated version is not stiff enough to reproduce a $2 M_{\odot}$ neutron star.

However, even if it turns out that finally, all these components are absent from cold neutron stars, they could be populated at finite temperature due to thermal effects. Within this paper, we have discussed results for several phenomenological EoS models containing hyperons and/or pions at finite temperature and for various hadronic charge fractions Y_Q .

The models behave very differently concerning the cold neutron star EoS. They cover a large range of neutron star radii, maximum masses – not all of them are compatible with a maximum mass of $2M_{\odot}$ – and strangeness content. In particular, we have extended some recent RMF parameterizations from Ref. [26] to finite temperature which contain the complete baryon octet and which give radii of the order 12-13 km for a star with $M = 1.4M_{\odot}$, maximum masses above $2 M_{\odot}$ and a relatively important strangeness content.

Qualitatively similar results are obtained within all EoS models, independently of the underlying interaction. Major outcomes are that hyperons and/or pions can become abundant already at saturation density if the temperature exceeds roughly 25 MeV. Their abundance increases with decreasing Y_Q , too, leading to the possibility of meta-stable hot proto-neutron stars and a delayed collapse to a black hole, see e.g. [116]. Let us emphasize that a more quantitative analysis of these results allowing to clarify the composition and thermodynamic properties of hot and dense baryonic matter would need additional constraints from future experimental data on hyperonic interactions and/or ab-initio calculations of baryonic matter with hyperons and mesons.

Acknowledgments

This work has been partially funded by the SN2NS project ANR-10-BLAN-0503 and by Project PESt-OE/FIS/UI0405/2014 developed under the initiative QREN financed by the UE/FEDER through the program COMPETE/FCT, and it has been supported by NewCompstar, COST Action MP1304. Ad. R. R acknowledges partial support from the Romanian National Authority for Scientific Research under grants PN-II-ID-PCE-2011-3-0092 and PN 09 37 01 05 and kind hospitality from LPC-Caen and LUTH-Meudon.

References

1. W. Hillebrandt, K. Nomoto, R.G. Wolff, *Astron.Astrophys.* **133**, 175 (1984)
2. J.M. Lattimer, F.D. Swesty, *Nucl.Phys.* **A535**, 331 (1991)
3. H. Shen, H. Toki, K. Oyamatsu, K. Sumiyoshi, *Nucl. Phys. A* **637**, 435 (1998)
4. S. Blinnikov, I. Panov, M. Rudzsky, K. Sumiyoshi, *Astron.Astrophys.* **535**, A37 (2011), 0904.3849
5. S. Heckel, P.P. Schneider, A. Sedrakian, *Phys. Rev.* **C80**, 015805 (2009)
6. M. Hempel, J. Schaffner-Bielich, *Nucl. Phys.* **A837**, 210 (2010)

7. G. Shen, C. Horowitz, S. Teige, *Phys.Rev.* **C83**, 035802 (2011), 1101.3715
8. G. Shen, C.J. Horowitz, S. Teige, *Phys. Rev. C* **83**, 035802 (2011)
9. K. Sumiyoshi, G. Röpke, *Phys. Rev.* **C77**, 055804 (2008)
10. A.R. Raduta, F. Gulminelli, *Phys. Rev.* **C82**, 065801 (2010)
11. J. Antoniadis, P.C.C. Freire, N. Wex, T.M. Tauris, R.S. Lynch, M.H. van Kerkwijk, M. Kramer, C. Bassa, V.S. Dhillon, T. Driebe et al., *Science* **340**, 448 (2013), 1304.6875
12. P. Demorest, T. Pennucci, S. Ransom, M. Roberts, J. Hessels, *Nature* **467**, 1081 (2010), 1010.5788
13. N.K. Glendenning, *Phys. Lett.* **B114**, 392 (1982)
14. F. Hofmann, C. Keil, H. Lenske, *Phys.Rev.* **C64**, 025804 (2001)
15. J. Rikovska-Stone, P.A. Guichon, H.H. Matevosyan, A.W. Thomas, *Nucl.Phys.* **A792**, 341 (2007), nucl-th/0611030
16. I. Bednarek, P. Haensel, J. Zdunik, M. Bejger, R. Manka, *Astron.Astrophys.* **543**, A157 (2012), 1111.6942
17. S. Weissenborn, D. Chatterjee, J. Schaffner-Bielich, *Nucl.Phys.* **A881**, 62 (2012), 1111.6049
18. S. Weissenborn, D. Chatterjee, J. Schaffner-Bielich, *Phys.Rev.* **C85**, 065802 (2012), 1112.0234
19. L. Bonanno, A. Sedrakian, *Astron. Astrophys.* **539**, A16 (2012)
20. M. Oertel, A. Fantina, J. Novak, *Phys.Rev.* **C85**, 055806 (2012), 1202.2679
21. G. Colucci, A. Sedrakian, *Phys.Rev.* **C87**, 055806 (2013), 1302.6925
22. L.L. Lopes, D.P. Menezes, *Phys.Rev.* **C89(2)**, 025805 (2014), 1309.4173
23. S. Banik, M. Hempel, D. Bandyopadhyay, *Astrophys.J.Suppl.* **214**, 22 (2014), 1404.6173
24. E. van Dalen, G. Colucci, A. Sedrakian, *Phys.Lett.* **B734**, 383 (2014), 1406.0744
25. T. Katayama, K. Saito (2014), 1410.7166
26. M. Oertel, C. Providência, F. Gulminelli, A.R. Raduta, *J. Phys.* **G42(7)**, 075202 (2015), 1412.4545
27. I. Sagert, T. Fischer, M. Hempel, G. Pagliara, J. Schaffner-Bielich, A. Mezzacappa, F.K. Thielemann, M. Liebendörfer, *Phys. Rev. Lett.* **102**, 081101 (2009)
28. A. Sedrakian (2015), 1509.06986
29. F. Gulminelli, A. Raduta, M. Oertel, *Phys.Rev.* **C86**, 025805 (2012), 1206.4924
30. F. Gulminelli, A. Raduta, M. Oertel, J. Margueron, *Phys.Rev.* **C87(5)**, 055809 (2013), 1301.0390
31. J. Schaffner-Bielich, A. Gal, *Phys.Rev.* **C62**, 034311 (2000), nucl-th/0005060
32. J. Torres, work in progress (2015)
33. D. Chatterjee, I. Vidana (2015), 1510.06306
34. N.K. Glendenning, *Phys. Rev.* **D46**, 1274 (1992)
35. P. Chomaz, F. Gulminelli, *European Physical Journal A* **30**, 317 (2006)
36. C. Ducoin, P. Chomaz, F. Gulminelli, *Nucl.Phys.* **A771**, 68 (2006), nucl-th/0512029
37. M.E. Gusakov, P. Haensel, E.M. Kantor, *Mon. Not. Roy. Astron. Soc.* **439(1)**, 318 (2014), 1401.2827
38. P. Chomaz, F. Gulminelli, C. Ducoin, P. Napolitani, K. Hasnaoui, *Phys.Rev.* **C75**, 065805 (2007), astro-ph/0507633
39. C. Providencia, L. Brito, S. Avancini, D. Menezes, P. Chomaz, *Phys.Rev.* **C73**, 025805 (2006)
40. M. Barranco, J.R. Buchler, *Phys.Rev.* **C24**, 1191 (1981)
41. F. Douchin, P. Haensel, J. Meyer, *Nucl.Phys.* **A665**, 419 (2000)
42. S. Balberg, A. Gal, *Nucl. Phys.* **A625**, 435 (1997)
43. P. Khaustov et al. (AGS E885), *Phys. Rev.* **C61**, 054603 (2000)
44. I. Vidaña, A. Polls, A. Ramos, H.J. Schulze, *Phys. Rev.* **C64**, 044301 (2001)
45. A. et al., *Phys. Rev.* **C88**, 014003 (2013)
46. B. Peres, M. Oertel, J. Novak, *Phys.Rev.* **D87**, 043006 (2013), 1210.7435
47. A.R. A. Polls, I.V. na, *Phys. Rev.* **C65**, 035804 (2002)
48. I.V.n. J. Margueron, I. Bombaci, *Phys. Rev.* **C68**, 055806 (2003)
49. N. Iwamoto, C. Pethick, *Phys. Rev.* **D25**, 313 (1982)
50. E.H. J. Navarro, D. Vautherin, *Phys. Rev.* **C60**, 045801 (1999)
51. A. Fetter, J. Walecka, Quantum theory of many-particle systems (McGraw-Hill, New York, 1971)
52. M.P. S. Reddy, J. Lattimer, *Phys. Rev.* **D58**, 013009 (1998)
53. J.M. C. Ducoin, P. Chomaz, *Nucl. Phys. A* **809**, 30 (2008)
54. M. Prakash, I. Bombaci, M. Prakash, P.J. Ellis, J.M. Lattimer et al., *Phys.Rept.* **280**, 1 (1997), nucl-th/9603042
55. J.A. Pons, J.A. Miralles, M. Prakash, J.M. Lattimer, *Astrophys.J.* **553**, 382 (2001), astro-ph/0008389
56. J.A. Pons, S. Reddy, P.J. Ellis, M. Prakash, J.M. Lattimer, *Phys.Rev.* **C62**, 035803 (2000), nucl-th/0003008
57. I. Bombaci, D. Logoteta, C. Providencia, I. Vidana, *Astron.Astrophys.* **462**, 1017 (2007), 1102.1665
58. D.P. Menezes, C. Providencia (2007), astro-ph/0703649
59. V. Dexheimer, S. Schramm, *Astrophys.J.* **683**, 943 (2008), 0802.1999
60. N. Yasutake, K. Kashiwa, *Phys. Rev. D* **79(4)**, 043012 (2009)
61. C. Ishizuka, A. Ohnishi, K. Tsubakihara, K. Sumiyoshi, S. Yamada, *J. Phys. G* **35**, 085201 (2008)
62. K. Nakazato, K. Sumiyoshi, S. Yamada, *Phys. Rev. D* **77(10)**, 103006 (2008)
63. I. Sagert, T. Fischer, M. Hempel, G. Pagliara, J. Schaffner-Bielich et al., *Acta Phys.Polon.* **B43**, 741 (2012), 1112.6328
64. M. Buballa et al., *J. Phys.* **G41(12)**, 123001 (2014), 1402.6911
65. M. Alford, D. Blaschke, A. Drago, T. Klähn, G. Pagliara et al., *Nature* **445**, E7 (2007), astro-ph/0606524
66. O.E. Nicotra, M. Baldo, G.F. Burgio, H.J. Schulze, *Phys. Rev. D* **74(12)**, 123001 (2006), astro-ph/0608021
67. G.F. Burgio, H.J. Schulze, A. Li, *Phys. Rev.* **C83**, 025804 (2011)
68. H. Chen, M. Baldo, G.F. Burgio, H.J. Schulze, *Phys. Rev. D* **86(4)**, 045006 (2012), 1203.0158
69. R.W. Mayle, J.R. Wilson, M. Tavani, *Astrophys. J.* **418**, 398 (1993)
70. M. Dutra, O. Lourenço, S. Avancini, B. Carlson, A. Delfino et al., *Phys.Rev.* **C90(5)**, 055203 (2014), 1405.3633
71. N.K. Glendenning, S.A. Moszkowski, *Phys. Rev. Lett.* **67**, 2414 (1991)
72. Y. Sugahara, H. Toki, *Nucl. Phys. A* **579**, 557 (1994)

73. C. Providencia, A. Rabhi, *Phys. Rev.* **C87**(5), 055801 (2013), 1212.5911
74. S.S. Avancini, L. Brito, J.R. Marinelli, D.P. Menezes, M.M.W. de Moraes, C. Providencia, A.M. Santos, *Phys. Rev.* **C79**, 035804 (2009), 0812.3170
75. T. Gaitanos, M. Di Toro, S. Typel, V. Baran, C. Fuchs, V. Greco, H.H. Wolter, *Nucl. Phys.* **A732**, 24 (2004), [nucl-th/0309021](#)
76. S. Typel, G. Röpke, T. Klähn, D. Blaschke, H. Wolter, *Phys.Rev.* **C81**, 015803 (2010), 0908.2344
77. J.M. Lattimer, F.D. Swesty, *Nucl. Phys. A* **535**, 331 (1991)
78. T. Krüger, I. Tews, K. Hebeler, A. Schwenk, *Phys.Rev.* **C88**, 025802 (2013), 1304.2212
79. C.J. Horowitz, J. Piekarewicz, *Phys.Rev.* **C64**, 062802 (2001), [nucl-th/0108036](#)
80. J. Carriere, C. Horowitz, J. Piekarewicz, *Astrophys.J.* **593**, 463 (2003), [nucl-th/0211015](#)
81. R. Cavagnoli, D.P. Menezes, C. Providencia, *Phys. Rev.* **C84**, 065810 (2011), 1108.1733
82. J.M. Lattimer, Y. Lim, *Astrophys.J.* **771**, 51 (2013), 1203.4286
83. H. Shen, H. Toki, K. Oyamatsu, K. Sumiyoshi, *Astrophys.J.Suppl.* **197**, 20 (2011), 1105.1666
84. T. Miyatsu, M.K. Cheoun, K. Saito, *Phys. Rev.* **C88**(1), 015802 (2013), 1304.2121
85. J. Schaffner, I.N. Mishustin, *Phys.Rev.* **C53**, 1416 (1996), [nucl-th/9506011](#)
86. J.R. Torres, F. Gulminelli, D.P. Menezes (2015), 1510.01381
87. E. Khan, J. Margueron, F. Gulminelli, A.R. Raduta, *Phys. Rev.* **C92**(4), 044313 (2015)
88. J. Zdunik, P. Haensel, *Astron.Astrophys.* **551**, A61 (2013), 1211.1231
89. M. Fortin, J.L. Zdunik, P. Haensel, M. Bejger, *Astron. Astrophys.* **576**, A68 (2015), 1408.3052
90. F. Özel, D. Psaltis, T. Guver, G. Baym, C. Heinke et al. (2015), 1505.05155
91. A. Fedoseew, H. Lenske, *Phys. Rev. C* **91**(3), 034307 (2015), 1407.2643
92. C.C. Moustakidis, C.P. Panos, *Phys. Rev. C* **79**(4), 045806 (2009), 0805.0353
93. F. Anthea, private communication (2015)
94. A. Rabhi, P.K. Panda, C. Providencia, *Phys. Rev.* **C84**, 035803 (2011), 1105.0254
95. K. Sumiyoshi, C. Ishizuka, A. Ohnishi, S. Yamada, H. Suzuki, *Astrophys. J. Lett.* **690**, L43 (2009)
96. P. Char, S. Banik, D. Bandyopadhyay, *Astrophys. J.* **809**(2), 116 (2015), 1508.01854
97. A. Steiner, M. Prakash, J.M. Lattimer, *Phys. Lett.* **B486**, 239 (2000), [nucl-th/0003066](#)
98. J.A. Pons, S. Reddy, M. Prakash, J.M. Lattimer, J.A. Miralles, *Astrophys. J.* **513**, 780 (1999), [astro-ph/9807040](#)
99. G. Lugones, O.G. Benvenuto, *Phys. Rev. D* **58**(8), 083001 (1998)
100. A.W. Steiner, M. Prakash, J.M. Lattimer, *Phys. Lett. B* **486**, 239 (2000), [nucl-th/0003066](#)
101. G.y. Shao, *Phys. Lett. B* **704**, 343 (2011), 1109.4340
102. S. Rosswog, *Int. J. Mod. Phys. D* **24**, 1530012 (2015), 1501.02081
103. J.A. Faber, F.A. Rasio, *Living Rev.Rel.* **15**, 8 (2012), 1204.3858
104. M. Shibata, K. Taniguchi, *Living Rev.Rel.* **14**, 6 (2011)
105. Y. Sekiguchi, K. Kiuchi, K. Kyutoku, M. Shibata, *Phys.Rev.Lett.* **107**, 211101 (2011), 1110.4442
106. A. Bauswein, H. Janka, K. Hebeler, A. Schwenk, *Phys.Rev.* **D86**, 063001 (2012), 1204.1888
107. A. Bauswein, T. Baumgarte, H.T. Janka, *Phys.Rev.Lett.* **111**(13), 131101 (2013), 1307.5191
108. A. Bauswein, N. Stergioulas, H.T. Janka, *Phys.Rev.* **D90**(2), 023002 (2014), 1403.5301
109. A. Bauswein, N. Stergioulas, *ArXiv e-prints* (2015), 1502.03176
110. J.S. Read, L. Baiotti, J.D.E. Creighton, J.L. Friedman, B. Giacomazzo et al., *Phys.Rev.* **D88**, 044042 (2013), 1306.4065
111. C.L. Fryer, K. Belczynski, E. Ramirez-Ruiz, S. Rosswog, G. Shen, A.W. Steiner, *ArXiv e-prints* (2015), 1504.07605
112. S. Lawrence, J.G. Tervala, P.F. Bedaque, M.C. Miller (2015), 1505.00231
113. S. Wanajo, Y. Sekiguchi, N. Nishimura, K. Kiuchi, K. Kyutoku et al., *Astrophys.J.* **789**, L39 (2014), 1402.7317
114. Y. Sekiguchi, K. Kiuchi, K. Kyutoku, M. Shibata, *Phys. Rev. D* **91**(6), 064059 (2015), 1502.06660
115. H.T. Janka, K. Langanke, A. Marek, G. Martinez-Pinedo, B. Mueller, *Phys.Rept.* **442**, 38 (2007), [astro-ph/0612072](#)
116. J.A. Pons, A.W. Steiner, M. Prakash, J.M. Lattimer, *Phys. Rev. Lett.* **86**, 5223 (2001), [astro-ph/0102015](#)
117. K. Nakazato, K. Sumiyoshi, H. Suzuki, S. Yamada, *Phys. Rev.* **D81**, 083009 (2010)
118. Y. Sekiguchi, M. Shibata, *Astrophys.J.* **737**, 6 (2011), 1009.5303
119. W. Keil, H.T. Janka, *Astron. Astrophys.* **296**, 145 (1995)
120. T.W. Baumgarte, S.A. Teukolsky, S.L. Shapiro, H.T. Janka, W. Keil, *Astrophys. J.* **468**, 823 (1996)
121. K. Nakazato, S. Furusawa, K. Sumiyoshi, A. Ohnishi, S. Yamada, H. Suzuki, *Astrophys. J.* **745**, 197 (2012)
122. K. Nakazato, K. Sumiyoshi, S. Yamada, *Astrophys. J.* **721**, 1284 (2010)
123. K. Nakazato, K. Sumiyoshi, S. Yamada, *Astron. Astrophys.* **558**, A50 (2013), 1309.3383
124. A. Ohnishi, H. Ueda, T. Nakano, M. Ruggieri, K. Sumiyoshi, *Phys.Lett.* **B704**, 284 (2011), 1102.3753
125. M. Hempel, T. Fischer, J. Schaffner-Bielich, M. Liebendörfer, *Astrophys.J.* **748**, 70 (2012), 1108.0848
126. A.W. Steiner, M. Hempel, T. Fischer, *Astrophys.J.* **774**, 17 (2013), 1207.2184